

7777 FILE D 27

AD-A215 059

MEASUREMENT OF FLUCTUATIONS IN TILT OF ARCTIC ICE  
AT THE CEAREX OCEANOGRAPHY CAMP:  
EXPERIMENT REVIEW, DATA CATALOG, AND PRELIMINARY RESULTS

by

Peter V. Czipott and Walter N. Podney

Final Technical Report PD-LJ-89-369R  
Contract Number N00014-89-C-0087

Submitted to:

John G. Heacock, Code 1125GG  
Office of Naval Research  
800 N. Quincy Street  
Arlington, VA 22217-5000

Submitted by:

Physical Dynamics, Inc.  
7855 La Jolla Avenue, Suite 300  
La Jolla, CA 92037

September 1989

DTIC  
ELECTED  
DEC 04 1989  
S E D  
Q E

89 11 27 136

## ACKNOWLEDGEMENTS

Success of the CEAREX tiltmeter experiment depends on many people. We thank Dr. Philip Selwyn of the Office of Naval Technology for his interest that enabled the experiment to proceed. We also thank the Scott Polar Research Institute group including Peter Wadhams, Robin Williams, and Stuart Moore, whose offer to share allocated time at the ice camp made our participation feasible. Robin Williams monitored the signals and maintained the data acquisition system while one of us (PVC) languished in Longyearbyen, Svalbard. The Polar Science Center Logistics Group headed by Andy Heiberg smoothed the way for our participation at short notice. Their efforts contributed crucially to the success of the endeavor and to the pleasure of the experience. Chief scientist Jamie Morison approved our limited participation at the ice camp; he and camp manager Mike Welch ensured that the camp functioned both enjoyably and efficiently. Discussions with the scientists at the ice camp enhanced our understanding of physical processes in the Arctic; we look forward to collaborating on interdisciplinary studies using their results together with the tilt data. We acknowledge enlightening discussions with Peter Wadhams both prior to and after the experiment. We are grateful to Murray Levine who has graciously shared his thermistor data with us. Finally, we particularly thank John Heacock of the Office of Naval Research for his careful review of a draft of this report that resulted in significant improvements.

## ABSTRACT

Three tiltmeters set in a triangular array on the eastern Arctic Ocean near  $63^{\circ}$  N,  $10^{\circ}$  E produced data of high quality from 30 March 1989 through 19 April 1989, as part of the Coordinated Eastern Arctic Experiment (CEAREX). Spectra of tilt fluctuations show the same features as those from the Arctic Internal Wave Experiment (AIWEX), recorded in April 1985 on the Beaufort Sea near  $74^{\circ}$  N,  $145^{\circ}$  W. They show a spectral peak centered near a period of 40 seconds, which results from long period swell coming from open seas, together with a sharp rise in spectral density below a frequency of several cycles per hour, which comes from internal waves. A pronounced spectral valley or window, from about 2 mHz to 20 mHz, separates the two dominant features.

In addition to quasi-stationary fluctuations that give the dominant spectral features, the data reveal three kinds of intermittent activity: (1) solitary internal waves emanating from the direction of the Yermak Plateau, (2) seismic-like signals coming from ice rupture, and (3) rapid oscillations with periods of a few seconds, lasting for tens of minutes, that possibly arise from rigid oscillations of an ice floe driven by wind gusts. Fluctuations in tilt are highly coherent with *in situ* temperature fluctuations that come from a solitary internal wave packet, but fluctuations in strain show little coherence. Because tilt results predominantly from ice flexure and strain mainly from ice compression, internal waves probably drive only flexural waves in the ice. Compressional noise dominates ice strain at internal wave frequencies, originating perhaps from differential motions of the ice pack.

Accession For	
NOIS CM&I	
DTIC TAB	
Unannounced	
Justification	
By	
Distribution	
Availability Codes	
Dist	Avail and/or
	Special

A-1



## TABLE OF CONTENTS

1.0 INTRODUCTION	1
2.0 EXPERIMENT REVIEW	2
2.1 Instrumentation	2
2.2 Experiment plan	5
3.0 DATA CATALOG	8
3.1 Data log	8
3.2 Samples of tiltmeter time series	14
3.3 Spectra of tilt fluctuations	14
3.4 Tilt amplitude anomaly	18
3.5 Directional spectra and array coherences	22
3.6 Tilt, strain, and internal waves	36
3.7 Time series and spectra of ice events	38
4.0 SCIENTIFIC ISSUES AND REQUIRED ANALYSES	49
4.1 Spectral variability over different time scales	49
4.2 Internal wave and swell studies	49
4.3 Flexural and compressional waves	50
4.4 Ice events and local forcing of waves by wind	50
4.5 Tilt amplitude anomaly	50
4.6 Directional spectral analyses	51
5.0 CONCLUSION	52
6.0 REFERENCES	53

## 1.0 INTRODUCTION

Measurements of fluctuating tilt of the Arctic Ocean ice cover at the Coordinated Eastern Arctic Experiment (CEAREX) Oceanography Camp (O-camp) north of the Svalbard archipelago confirm the nature of background tilt spectra measured earlier on the Beaufort Sea. They, together with simultaneous measurements of ice strain and of the local internal wave field, promise to determine the response of the ice to internal waves and swell, and its effect on wave generation and propagation in the Arctic Ocean.

In 1985, as part of the Arctic Internal Wave Experiment (AIWEX), we fielded a superconductive magnetic gradiometer on the Beaufort Sea north of Alaska at about 74° N, 145° W [Czipott and Podney, 1985]. To support the magnetic measurements we deployed two tiltmeters, one on the gradiometer platform and the other directly on the ice. We find that the spectrum of ice tilt displays consistent features. A broad spectral peak centered at a period of about 40 seconds describes long-period swell, heavily damped by the ice, propagating from the open ocean. A sharp rise in the spectrum below a frequency of several cycles per hour appears to arise from internal waves [Podney and Czipott, 1986]. A pronounced spectral valley or window lies between the two, from about 2 mHz to 20 mHz.

Measurements by a group from Scott Polar Research Institute of ice strain fluctuations north of Svalbard during the *Fram 3* experiment show similar spectral features [Williams *et al.*, 1989]. Preliminary analysis of strain at internal wave frequencies suggested that internal waves generate compressional waves in the ice rather than flexural waves [Manley *et al.*, 1982]. If true, this result is anomalous as it requires a much higher drag coefficient for the ice than inferred from model estimates and other measurements. CEAREX data, however, show that at least one solitary internal wave packet produces flexural waves alone and that strain at internal wave frequencies is predominantly compressional noise caused by differential motion of the ice pack.

The CEAREX measurements offer the opportunity to obtain background spectra of ice tilt fluctuations at a different location from AIWEX. Comparisons between spectra on the Beaufort Sea and north of Fram Strait allow estimates of the variability of background tilt fluctuations during springtime from place to place in the Arctic Ocean. CEAREX also enables a study of the internal wave field simultaneously using tiltmeters, strainmeters, and oceanographic sensors. It offers the chance to determine the interaction between the ice cover and internal waves.

Herein we first review the CEAREX ice tilt experiment, describing instrumentation, deployment, and data recording protocol. Next we discuss the data obtained. A data log summarizes the data available from each sensor. Spectra obtained near the start, middle, and end of the experiment illustrate ice tilting at different times. Closer examination of some segments shows ice activity associated with neither swell nor internal waves, but possibly with ice cracking or distant ridging. Finally, we describe further data analysis and interdisciplinary study required to characterize the interaction between ice and ocean.

## 2.0 EXPERIMENT REVIEW

Our experiment plan called for deployment of three tiltmeters in an array colocated with the strainmeter array set up by Scott Polar Research Institute (SPRI) of the University of Cambridge in Great Britain. We planned for one person from Physical Dynamics (PDI) and one from SPRI to reach the CEAREX O-camp on 18 March to set up the electronics hut and the tiltmeter array by 20 March. At that time the PDI investigator would return to Longyearbyen in Svalbard, to stand by in case of difficulties with the experiment. This plan allowed completion of the experiment on the non-interfering basis stipulated for our participation.

Tiltmeters and data acquisition equipment were marshaled, repaired, tested, packaged, and sent by air freight to the CEAREX staging area in Longyearbyen in early March, 1989. Peter Czipott of PDI arrived there on 13 March. Truculent Norwegian customs officials in Tromso together with overladen flights to Svalbard delayed receipt of the equipment until the 27th. Parallel delays in finding a suitable site for the O-camp meant that we could still participate on the specified non-interfering basis. The investigator and equipment flew to O-camp on 28 March. By this point, the SPRI strain array had already been deployed and was collecting data. The tiltmeters were set up by 30 March, when data collection began. Camp position on this day was  $83^{\circ} 3.2' N$ ,  $9^{\circ} 53.3' E$ .

Once the tiltmeter array was operating, Czipott aided other projects at the O-camp. Together with Robin Williams of SPRI, he surveyed a square grid 400 m on a side at camp to mark drill hole locations for an ice thickness map. In addition, he worked a daily shift on the microstructure profile experiment of Dillon and Padman from OSU, filling in when a family emergency forced another of the OSU personnel to leave camp for several days. On 5 April, the camp reached full manpower and he retired to Longyearbyen to stand by. Robin Williams monitored the tiltmeter array and data collection. The array operated continuously, except for a few occasions described below, until 19 April 1989, when the camp was at  $82^{\circ} 29.7' N$ ,  $7^{\circ} 59.5' E$ . Figure 2.1 shows the region of the eastern Arctic traversed by the O-camp [American Geographical Society, 1975], while Figure 2.2 shows camp drift during CEAREX.

### 2.1 Instrumentation

We deployed three tiltmeters in a triangular array. Two tiltmeters are biaxial electrolytic bubble level meters manufactured by the Autonetics Division of Rockwell International (Model No. SE541ALRA-P120-11T, Serial Nos. 179C and 180C). They are the same tiltmeters deployed at AIWEX. A cavity with concave upper surface of spherical radius 12 inches is filled with conducting fluid, leaving a bubble. Changes in the position of the bubble are sensed by four electrodes forming two resistance bridges along orthogonal axes. AC bridge excitation and subsequent demodulation of the signal yield a voltage proportional to angular deflection from the vertical. The third tiltmeter, acquired for CEAREX, is manufactured by Applied Geomechanics, Inc. (Model No. 701-2A, Serial No. 928). It operates on the same principle, but uses a separate bent tube for each tilt axis. Table 1 presents output calibrations supplied by the manufacturers. Calibrations are given in millivolts per second of arc. One arc-sec equals  $4.85 \times 10^{-8}$  radians.

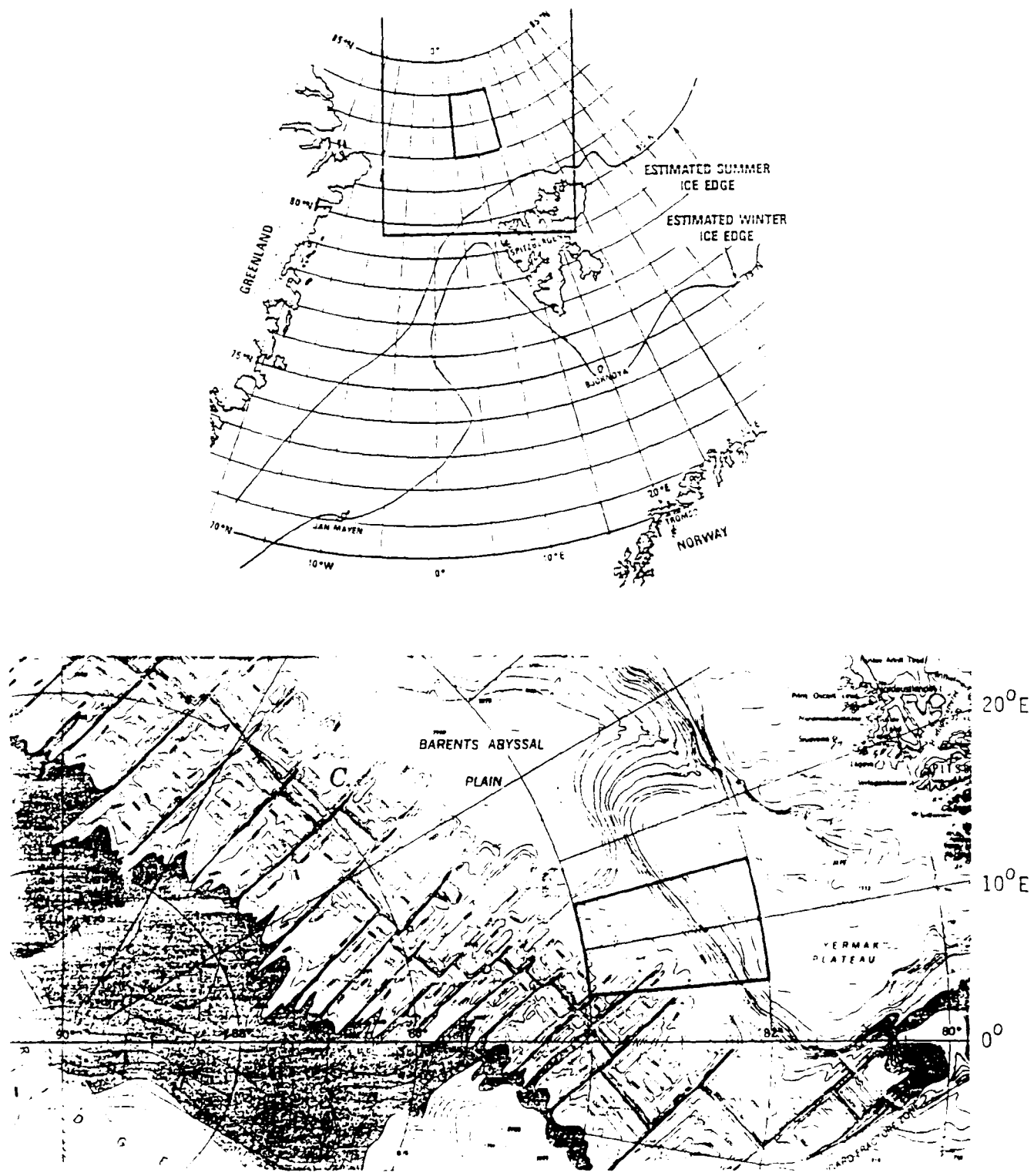


**FIGURE 2.1**

Index map of the eastern Arctic (top), outlining the area covered by a bathymetric map of the Arctic Ocean [American Geographical Society, 1975]. A heavy line borders the area over which the O-camp drifted during CEAREX and which is enlarged in Figure 2.2.

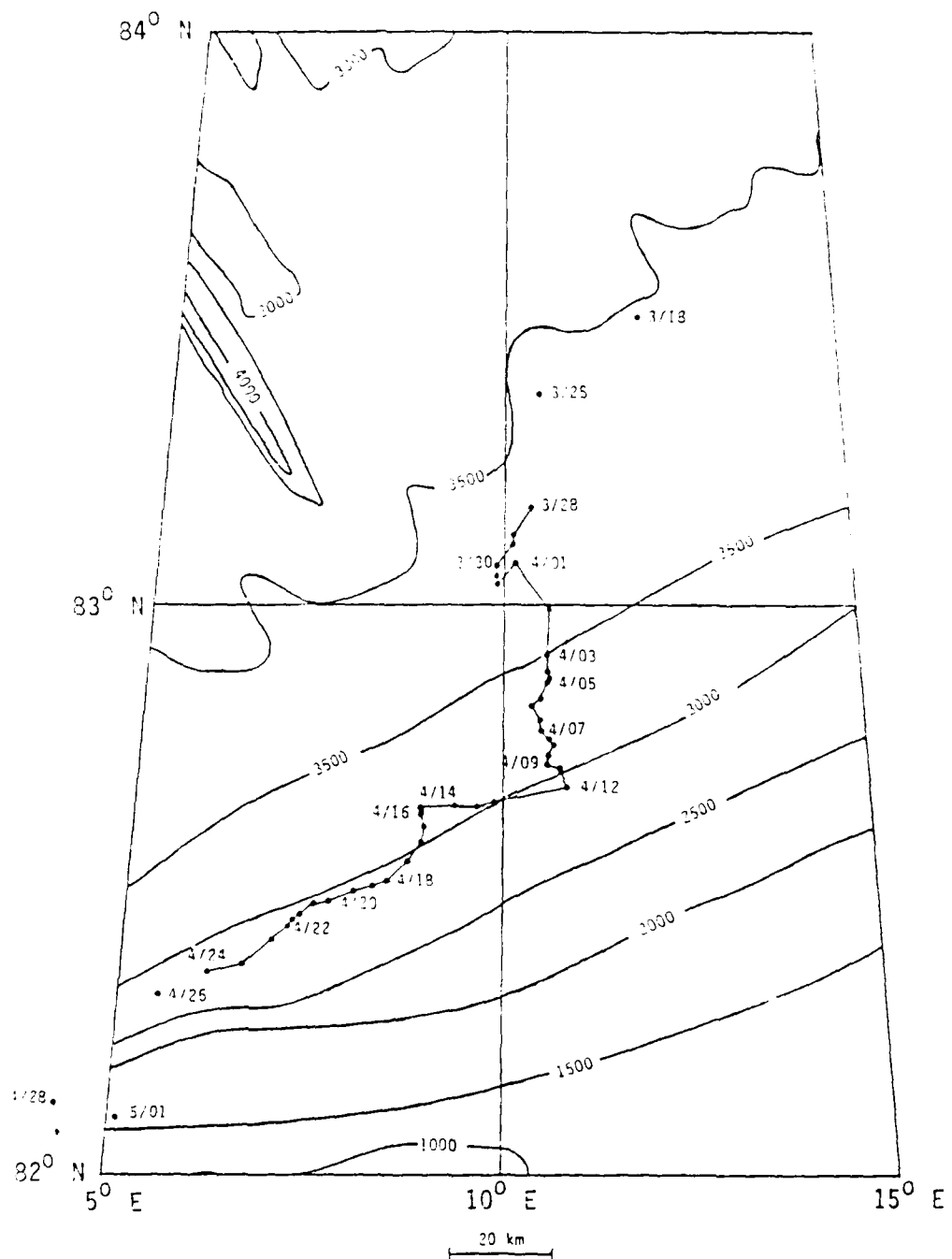


**FIGURE 2.2**

Detail map of the Arctic Ocean between  $82^{\circ}$  N and  $84^{\circ}$  N,  $5^{\circ}$  E and  $15^{\circ}$  E, showing position of the O-camp as a function of time [Andersen, 1989]. A line joins positions recorded less than 24 hours apart. Bathymetric contours are approximated from the map of Figure 2.1; depths are given in meters. Contours in the southern half indicate the edge of the Yermak Plateau; contours to the northwest show the edge of the mid-oceanic ridge.

**TABLE 1.**  
*TILTMETER GAINS in mV/arcsec*

<u>TILTMETER</u>	<u>SETTING</u>	<u>X AXIS</u>	<u>Y AXIS</u>
Rockwell 179C	—	55.09	55.46
Rockwell 180C	—	52.21	53.02
Appl. Geomech.	High gain	47.27	47.80

All three tiltmeters have temperature sensors incorporated into the housing, but only the Applied Geomechanics (AGI) sensor is functional. Its output is calibrated at 10 mV/ $^{\circ}$ C and reads zero voltage at 0  $^{\circ}$ C.

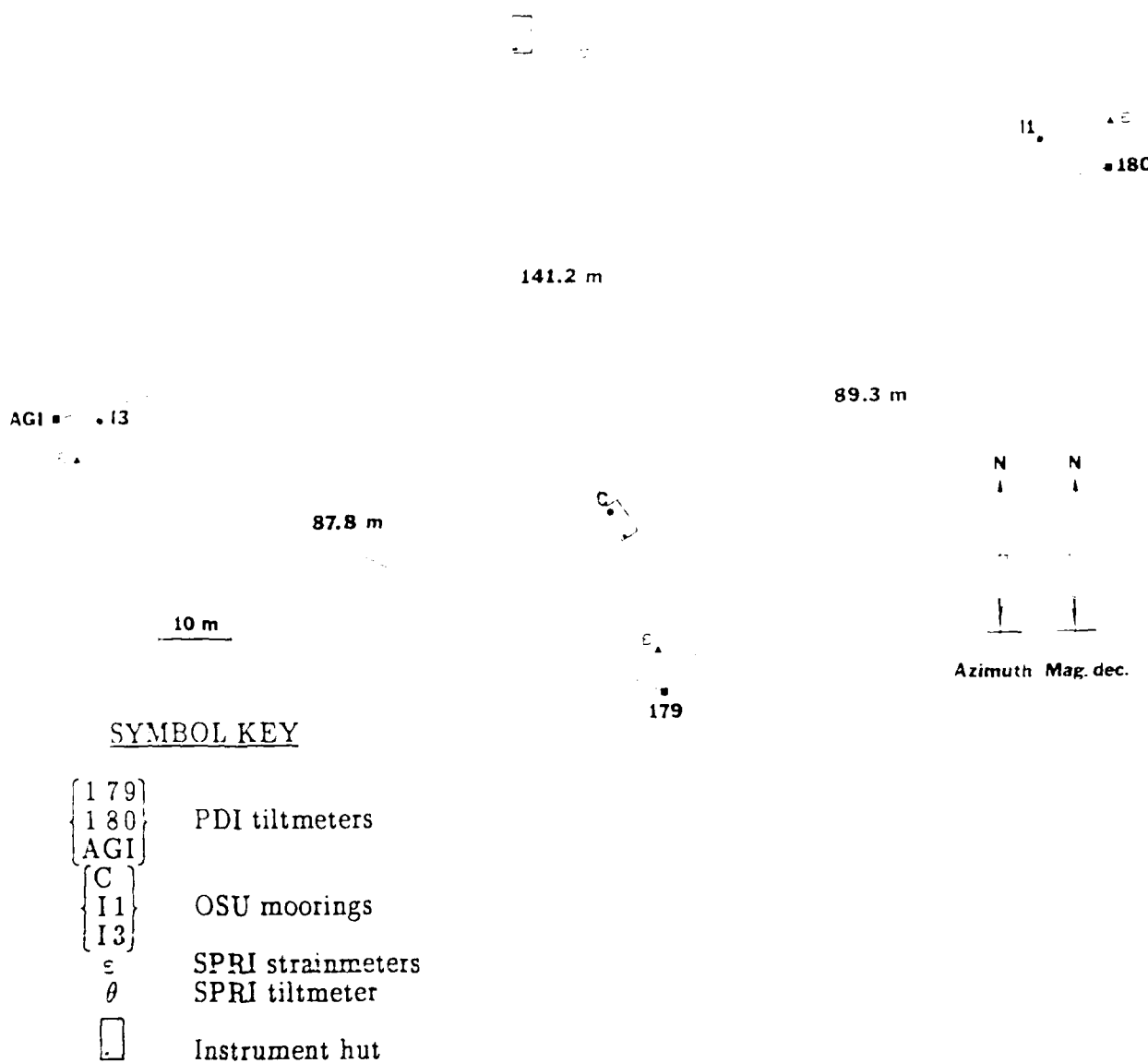
In addition to our sensors described above, we also record several outputs from the sensors deployed at CEAREX by SPRI [R. Williams, personal communication]. Their sensors include a bubble level tiltmeter installed near the instrument hut, as well as a triangular array of strainmeter rosettes. Each rosette consists of three strainmeters oriented at 120 $^{\circ}$  intervals in a plane. It measures principal axes of strain to within an ambiguity of 180 $^{\circ}$ . The triangular array removes the sign ambiguity. The strainmeter is an Invar wire one meter long, anchored to the ice at one end. The other end moves with respect to a measurement point also fixed to the ice. Extension or compression of the ice causes a changing displacement of the wire's free end that is measured with a Linear Velocity and Displacement Transducer (LVDT). We record three axes of strain from one rosette and one tilt axis.

Data Translation A-to-D cards in an IBM PC/XT computer digitize the data. A DT2801/5716 card provides 16 bit resolution for up to 8 channels, and a DT2801 digitizes up to 16 channels at 12 bit resolution. Input dynamic range can be set with software switches to  $\pm 10$ ,  $\pm 5$ ,  $\pm 2.5$ , or  $\pm 1.25$  volts. Data collection is controlled by Labtech Notebook software. Data are recorded on 10 Mbyte, 7 inch flexible disk cartridges.

## 2.2 Experiment Plan

Three sensor arrays are deployed near each other, as shown in Figure 2.3: our tiltmeter array, the SPRI strainmeter array, and the array of moored oceanographic sensors of Levine and Paulson from Oregon State University. The OSU array consists of a central mooring surrounded by two nested equilateral triangular moorings. Colocating the tilt and strain arrays ensures good coherence for point measurements of the dispersion relations for flexural and compressional waves propagating through the array. Placing the arrays near the OSU moorings allows the best chance of directly correlating ice motion to motion of the water below. Because of the hut location dictated by the camp layout, SPRI sited the three points of the tilt and strain arrays at the central mooring and two of the inner triangular moorings rather than at the three points of the inner triangle as originally envisaged.

The tiltmeter array forms a nearly isosceles triangle. Tiltmeters are identified as AGI (Applied Geomechanics, Inc.), 179, and 180 (Rockwell tiltmeters S/N 179C and 180C, respectively). The camp azimuth, a standard reference, was measured twice daily, weather permitting. Its heading varied between 234.2 $^{\circ}$  true and 243.8 $^{\circ}$  true during the tiltmeter experiment [Andersen, 1989]. Assuming a camp azimuth of 240 $^{\circ}$ , the heading from

**FIGURE 2.3**

Map of sensor arrays at the O-camp, taken from surveys conducted by M. Levine [personal communication] and P. Czipott. The map is drawn assuming a  $240^{\circ}$  camp azimuth. One marker of true north shows variations of camp azimuth while the PDI array operated. The other marker shows variations of magnetic declination during the same period.

tiltmeter 179 to tiltmeter 180 is  $40.2^\circ$  true. The two Rockwell tiltmeters are set up with the X-axis measuring tilt in the magnetic north-south plane; the AGI sensor, with the opposition labelling convention, uses the Y-axis to measure north-south tilt. (Magnetic declination varied between  $-6^\circ$  and  $-9^\circ$  during tiltmeter setup.) Because of unevenness of the ice surface, tiltmeters are not precisely aligned with magnetic north. Within a measurement error of  $\pm 2^\circ$ , the nominal north-south tilt axis of tiltmeter 179 points  $2^\circ$  west of magnetic north, 180 points due magnetic north, and AGI points  $13^\circ$  west of magnetic north as measured on 30 March.

Data are recorded at a sampling rate of 1 Hz in the configuration shown in Table 2. They are anti-aliased using 4-pole Butterworth filters with the indicated cutoff frequency. Additional sensors are identified as SPRI (SPRI tiltmeter, located near the electronics hut) and II (strainmeters near OSU mooring II, oriented as indicated with respect to North).

TABLE 2.  
CHANNEL IDENTIFICATIONS

SENSOR	A/D RES. (bits)	CHANNEL NO.	CUTOFF (Hz)
AGI Temp.	16	0	0.005
AGI X axis (E-W)	16	1	0.250
AGI Y axis (N-S)	16	2	0.250
179 X axis (N-S)	16	3	0.250
179 Y axis (E-W)	16	4	0.250
180 X axis (N-S)	16	5	0.250
180 Y axis (E-W)	16	6	0.250
SPRI N-S tilt	16	7	0.250
II strain ( $0^\circ$ )	12	0	—
II strain ( $120^\circ$ )	12	1	—
II strain ( $240^\circ$ )	12	2	—

Electrical power comes to the hut over a 200 m long, three-conductor, 10 gauge cable from the main camp generator. One conductor is neutral, and the other two are at  $\pm 120$  VAC. The neutral is connected via copper braid to seawater ground at the hut. One side is designated as "clean" power (for sensitive electronics), and the other as "dirty" (for winches, battery chargers, and appliances). At the hut, clean power ran at about 105 VAC, while dirty ran at 115 VAC. Because of the low voltage on the clean side, we ran the electronics from dirty power, using a Topaz Powermaker Micro UPS to condition the line signal and to provide continuity during the twice-daily generator shutdowns. A surge suppressor on the UPS output further protected the electronics.

Labtech Notebook can merge up to five channels into a single data file. We set up three data files for each data interval. The first file contains the first five channels listed in the table, and the next two contain three channels, each. Under normal operating conditions, we start a new set of files each day. Data are written to disk continuously, but Labtech Notebook only closes the data files once, at the end of a run. This means that until the run's end the data are vulnerable to a computer or power failure. By ending a run each day we ensure that not too much data is subject to loss. Files are tagged with the Julian number of the start day and a letter (A,B,C,...) indicating the sequence when more than one run is started in a given day.

### 3.0 DATA CATALOG

In this section we catalog data read from the files thus far. We then present an overview of the tilt time series; show spectra of tilt fluctuations; discuss some discrete events recorded by the tiltmeters; and finally present preliminary analyses of directional spectra and array coherences.

#### 3.1 Data log

Data files are nearly continuous except for a few gaps. Otherwise, data records are interrupted for a few minutes between the end of one file and the start of the next. Table 3 lists existing data files and points out gaps in the data exceeding one hour in length. Shorter gaps, not listed, are caused by precautionary system shutdowns during generator oil changes, backing up data disks, and the like. All times are presented as Julian day:hour:minute:second referred to Universal Time (UT).

TABLE 3.  
DATA FILE CATALOG

DATE	FILE	START TIME	POINTS/CHAN	END TIME
30 March	089A	089:22:09:00	31500	090:06:54:00
	—	<i>analyzing data to ensure that instruments are operating</i>		
31	090A	090:23:10:00	34979	091:08:52:59
01 April	091A	091:09:08:00	78797	092:07:01:17
02	092A	092:07:05:00	86069	093:06:59:29
03	093A	093:07:03:00	21770	093:13:05:50
03	093B	093:13:36:00	62679	094:07:00:39
	—	<i>write fault errors on disk; data lost</i>		
04	094C	094:10:18:00	83458	095:09:28:58
	—	<i>training Williams on Labtech Notebook; data exists</i>		
05	095C	095:10:42:00	73555	096:07:07:55
06	096A	096:07:15:00	86013	097:07:08:33
	—	<i>lengthy power outage causes UPS failure; data lost</i>		
07	097D	097:17:52:00	48158	098:07:14:38
08	098A	098:07:19:00	86014	099:07:02:34
09	099A	099:07:26:00	86112	100:07:21:12
10	100A	100:07:27:00	86198	101:07:23:38
11	101A	101:07:28:00	23206	101:13:54:46
11	101B	101:14:22:00	60261	102:07:06:21
12	102A	102:07:15:00	86198	103:07:11:38
13	103A	103:07:21:00	12208	103:10:44:28
13	103B	103:11:17:00	71578	104:07:09:58
14	104A	104:07:24:00	19860	104:12:55:00
14	104B	104:13:39:00	63379	105:07:15:19
15	105A	105:07:19:00	30239	105:15:42:59
	—	<i>UPS failure; data recoverable</i>		
16	106B	106:12:53:00	21719	106:18:54:59
16	106C	106:19:08:00	42553	107:06:57:13
	—	<i>UPS failure; data lost</i>		
17	107B	107:19:14:00	42137	108:06:58:17
18	108A	108:07:15:00	42006	108:18:55:06
18	108B	108:19:09:00	42406	109:06:55:46
19	109A	109:07:13:00	13690	109:11:01:10

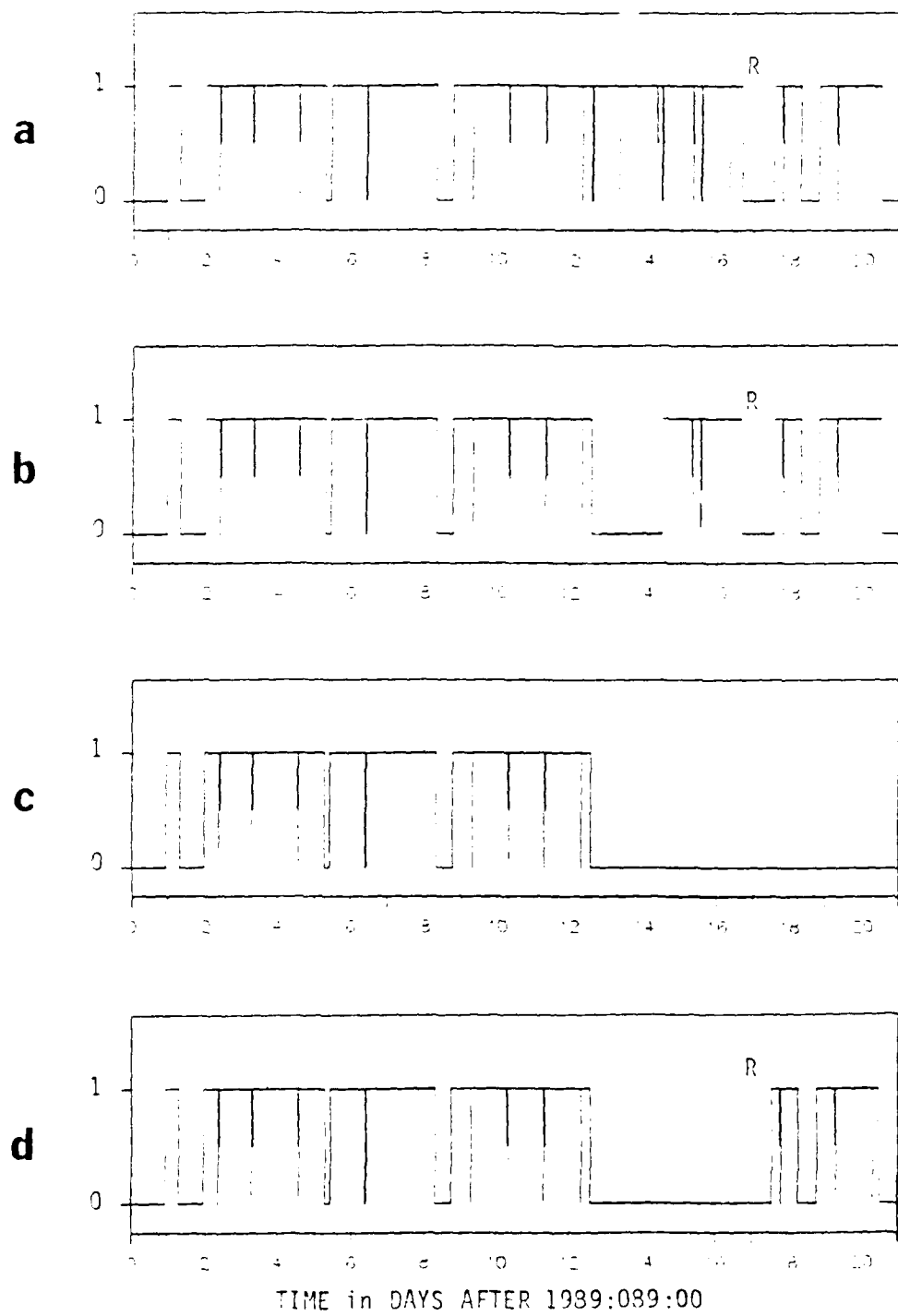
On 12 April, Robin Williams reported that a warm front arriving the previous day, associated with strong winds, had caused one tiltmeter channel to drift beyond the A-to-D input dynamic range. He reset the input ranges on 13 April, and radioed an urgent call for Peter Czippott to fly to camp to correct possible malfunctions. Inclement weather delayed his arrival until the 15th. He found that the new range settings had brought the signals satisfactorily back onscale. Unfortunately, the AGI tiltmeter outputs saturate at  $\pm 8$  volts, not  $\pm 10$ . Thus, even though the signal was onscale within the A-to-D dynamic range, the tilt had exceeded the sensor's dynamic range. The tiltmeter needed either mechanical releveling on the ice or reducing the output amplifier gain. This was not done, and as a consequence, the north-south tilt axis of the AGI tiltmeter produced no useful data after 11 April or day 101. A problem discovered and corrected on the 15th was that an erroneous keystroke in operating Labtech Notebook had caused the SFRI strainmeters not to be recorded from the 11th to the 15th. Table 4 shows missing or offscale data in each file as a zero; complete data are indicated by a one.

TABLE 4.  
DATA AVAILABILITY BY FILE AND CHANNEL

FILE	AGI TEMP	AGI X	AGI Y	179C X	179C Y	180C X	180C Y	SFRI NS	SFRI E	SFRI 12S	SFRI 24S
99A	.	.	.	.	.	.	.	.	.	.	.
99A	.	.	.	.	.	.	.	.	.	.	.
99A	.	.	.	.	.	.	.	.	.	.	.
99A	.	.	.	.	.	.	.	.	.	.	.
99A	.	.	.	.	.	.	.	.	.	.	.
99B	.	.	.	.	.	.	.	.	.	.	.
99C	.	.	.	.	.	.	.	.	.	.	.
99D	.	.	.	.	.	.	.	.	.	.	.
99E	.	.	.	.	.	.	.	.	.	.	.
99F	.	.	.	.	.	.	.	.	.	.	.
99G	.	.	.	.	.	.	.	.	.	.	.
99H	.	.	.	.	.	.	.	.	.	.	.
99I	.	.	.	.	.	.	.	.	.	.	.
99J	.	.	.	.	.	.	.	.	.	.	.
99K	.	.	.	.	.	.	.	.	.	.	.
99L	.	.	.	.	.	.	.	.	.	.	.
99M	.	.	.	.	.	.	.	.	.	.	.
99N	.	.	.	.	.	.	.	.	.	.	.
99O	.	.	.	.	.	.	.	.	.	.	.
99P	.	.	.	.	.	.	.	.	.	.	.
99Q	.	.	.	.	.	.	.	.	.	.	.
99R	.	.	.	.	.	.	.	.	.	.	.
99S	.	.	.	.	.	.	.	.	.	.	.
99T	.	.	.	.	.	.	.	.	.	.	.
99U	.	.	.	.	.	.	.	.	.	.	.
99V	.	.	.	.	.	.	.	.	.	.	.
99W	.	.	.	.	.	.	.	.	.	.	.
99X	.	.	.	.	.	.	.	.	.	.	.
99Y	.	.	.	.	.	.	.	.	.	.	.
99Z	.	.	.	.	.	.	.	.	.	.	.
100A	.	.	.	.	.	.	.	.	.	.	.
101A	.	.	.	.	.	.	.	.	.	.	.
101B	.	.	.	.	.	.	.	.	.	.	.
102A	.	.	.	.	.	.	.	.	.	.	.
103A	.	.	.	.	.	.	.	.	.	.	.
103B	.	.	.	.	.	.	.	.	.	.	.
104A	.	.	.	.	.	.	.	.	.	.	.
104B	.	.	.	.	.	.	.	.	.	.	.
105A	.	.	.	.	.	.	.	.	.	.	.
106B	.	.	.	.	.	.	.	.	.	.	.
106C	.	.	.	.	.	.	.	.	.	.	.
107B	.	.	.	.	.	.	.	.	.	.	.
108A	.	.	.	.	.	.	.	.	.	.	.
108B	.	.	.	.	.	.	.	.	.	.	.
109A	.	.	.	.	.	.	.	.	.	.	.

Tables 3 and 4 show that from the start of data recording to the end of the experiment, we obtained 4115 sensor-hours of good data. Figure 3.1 presents the data log graphically as a binary time series which is high where data exists and low where it does not. A gap labelled "R" denotes data that are recoverable but not yet examined. Other gaps represent lost data. Spikes denote very short gaps between nearly continuous records.

Figures 3.2, 3.3 and 3.4 show time series on a secular scale of instrument temperature, tilting in the north-south plane, and tilting in the east-west plane. At the start, the temperature rises dramatically as snow drifts over the tiltmeters and insulates them. A later rise in temperature results after passage of a warm front and subsequent snowfall. The snow cover at the end of the experiment varied between 15 and 30 cm from one tiltmeter to another. East-west tilts show roughly correlated variations, although the large drift in one tiltmeter (179) occurs later and more suddenly than on the other two. The long-term variations of the north-south tilts are far less correlated. The north-south axis of the AGI tiltmeter shows variations highly correlated with temperature, suggesting

**FIGURE 3.1**

Time series representing recovered data (1) and data gaps (0). Spikes indicate gaps of only a few minutes' duration. One gap, labelled *R*, indicates recoverable data not yet processed. (a) All sensors except those specified below. (b) E-W axis, tiltmeter 180. (c) N-S axis, tiltmeter AGI. (d) All three SPRI strainmeters.

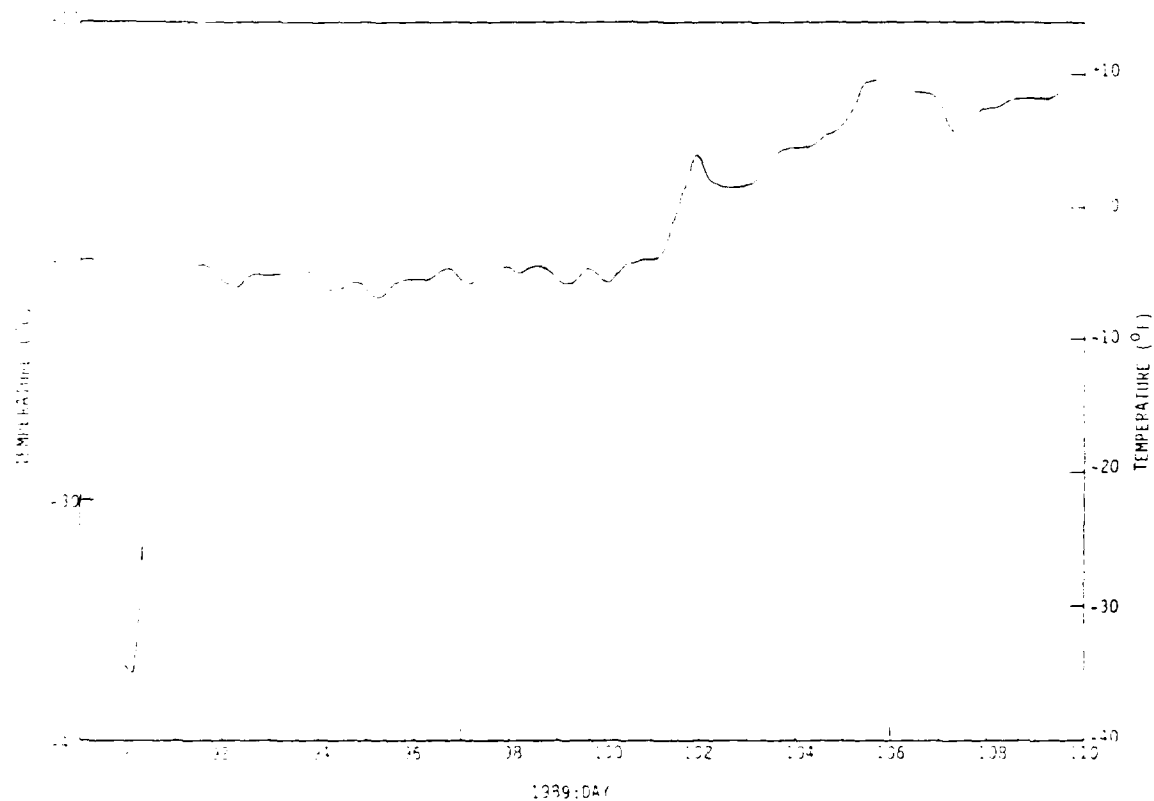


**FIGURE 3.2**

Secular time series of temperature inside tiltmeter AGI. Initial temperature equals ambient air temperature; as insulating snow drifts over the tiltmeter, temperature rises to a steady value near  $-20^{\circ}\text{ C}$ . A further secular change occurs during the passage of a warm front on 10–11 April.

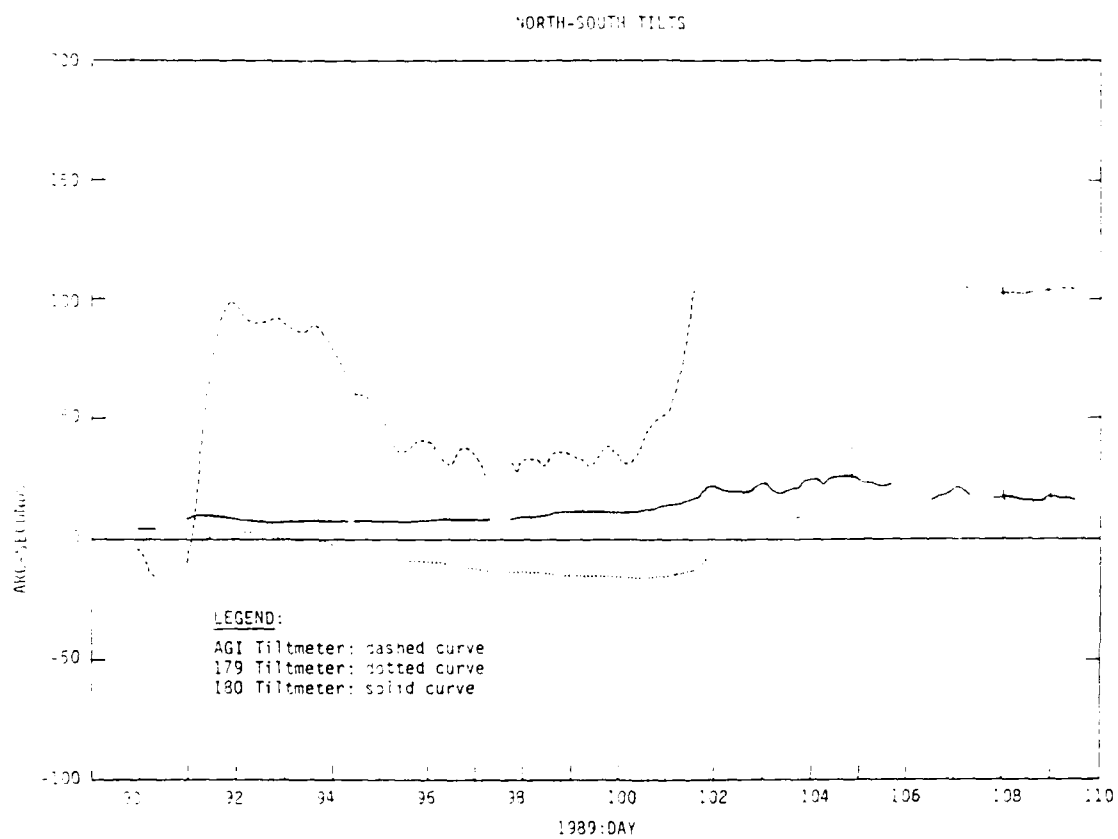


**FIGURE 3.3**

Secular time series of tilt in the north-south plane measured by the three PDI tiltmeters, indicated according to the legend. The AGI tiltmeter shows a much stronger correlation to temperature than the other sensors. Its tilt exceeded its dynamic range on 11 April.

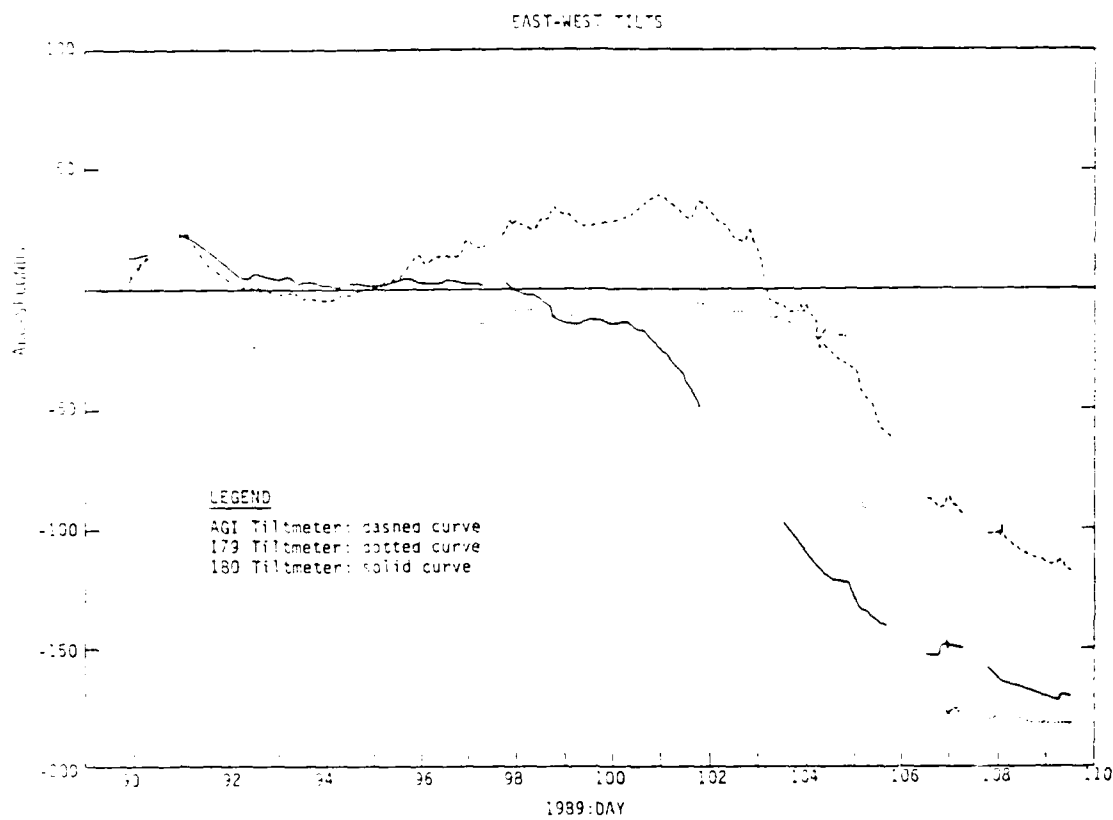


**FIGURE 3.4**

Secular time series of tilt in the east-west plane measured by the three PDI tiltmeters, indicated according to the legend. None of the signals shows a strong temperature correlation. All three measure a total excursion of similar magnitude although differing in the onset time of the large tilt variation. No simple picture of secular ice deformation emerges from the tiltmeter records.

an anomalously high temperature coefficient. The other axes show little correlation in north-south tilt. No simple picture of secular ice deformation emerges from considering all six tilts.

Analysis of time series generated by the SPRI tiltmeter and strainmeters is complicated by the fact that each sensor uses a servo motor to reset its output to zero automatically whenever it reaches a predetermined voltage. Thus, signals can be recorded with high resolution even in the presence of large excursions, and remain onscale. Time series, however, have numerous offsets that must be removed before the data can be analyzed. The problem is straightforward except during periods of large, high-frequency ice oscillations when distinguishing real variations from servo offsets becomes difficult.

### 3.2 Samples of tiltmeter time series

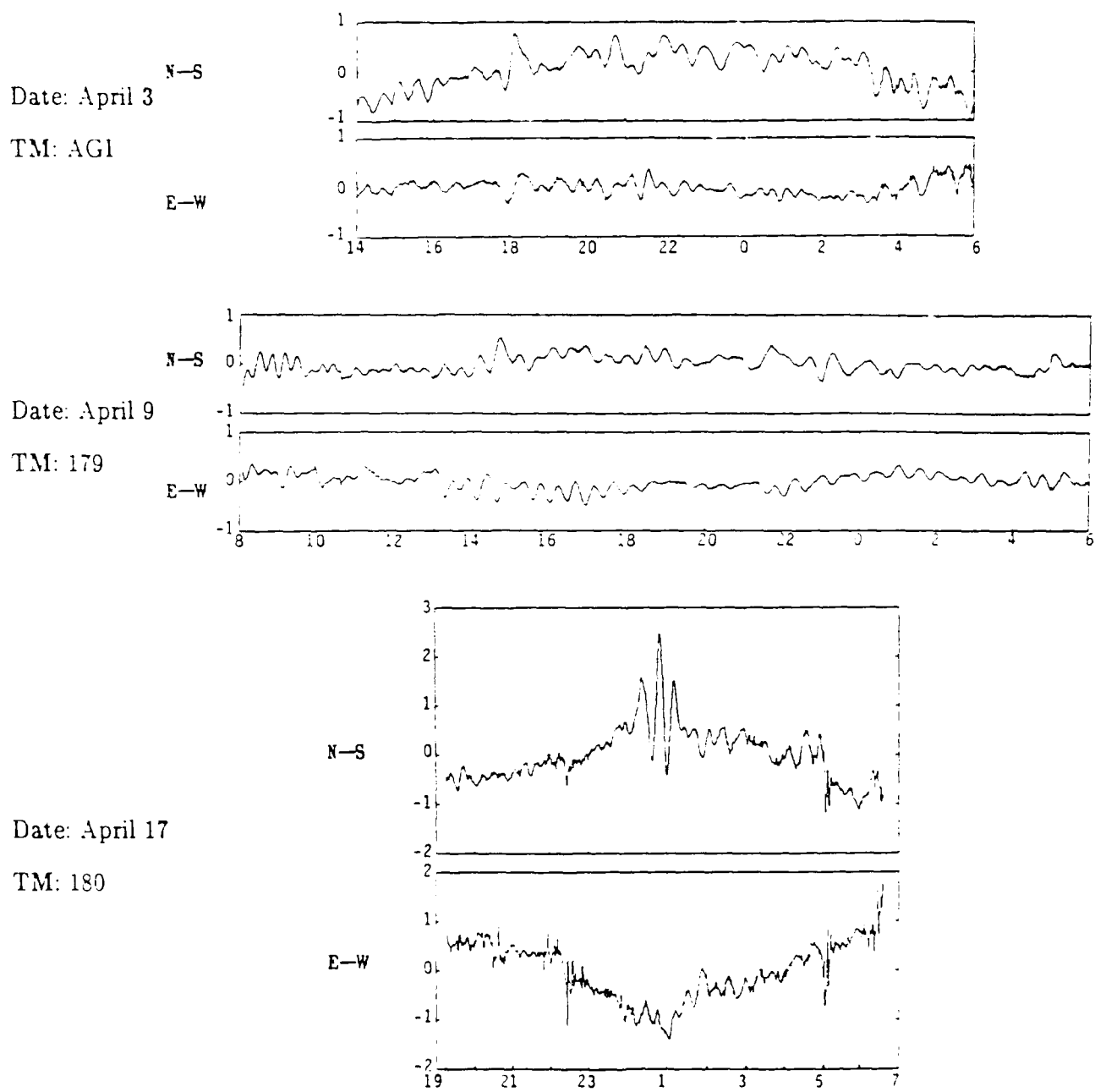
Internal waves cause fluctuations of the order of one to a few arcseconds in amplitude. Figure 3.5 shows time series segments from a few records. An internal wave train is clearly apparent in the segment from day 99. A strong solitary wave packet travels through the array on day 107. Section 3.5.2 discusses this data segment further. On some other days, internal wave fluctuations do not show such clear periodic behavior, indicating that the wave field then is not dominated by one mode.

Swell causes fluctuations of the order of an arcsecond in amplitude. Figure 3.6 shows short sections of time series from different days, displaying clear swell signals with the characteristic beating that results in wave packets or "sets".

### 3.3 Spectra of tilt fluctuations

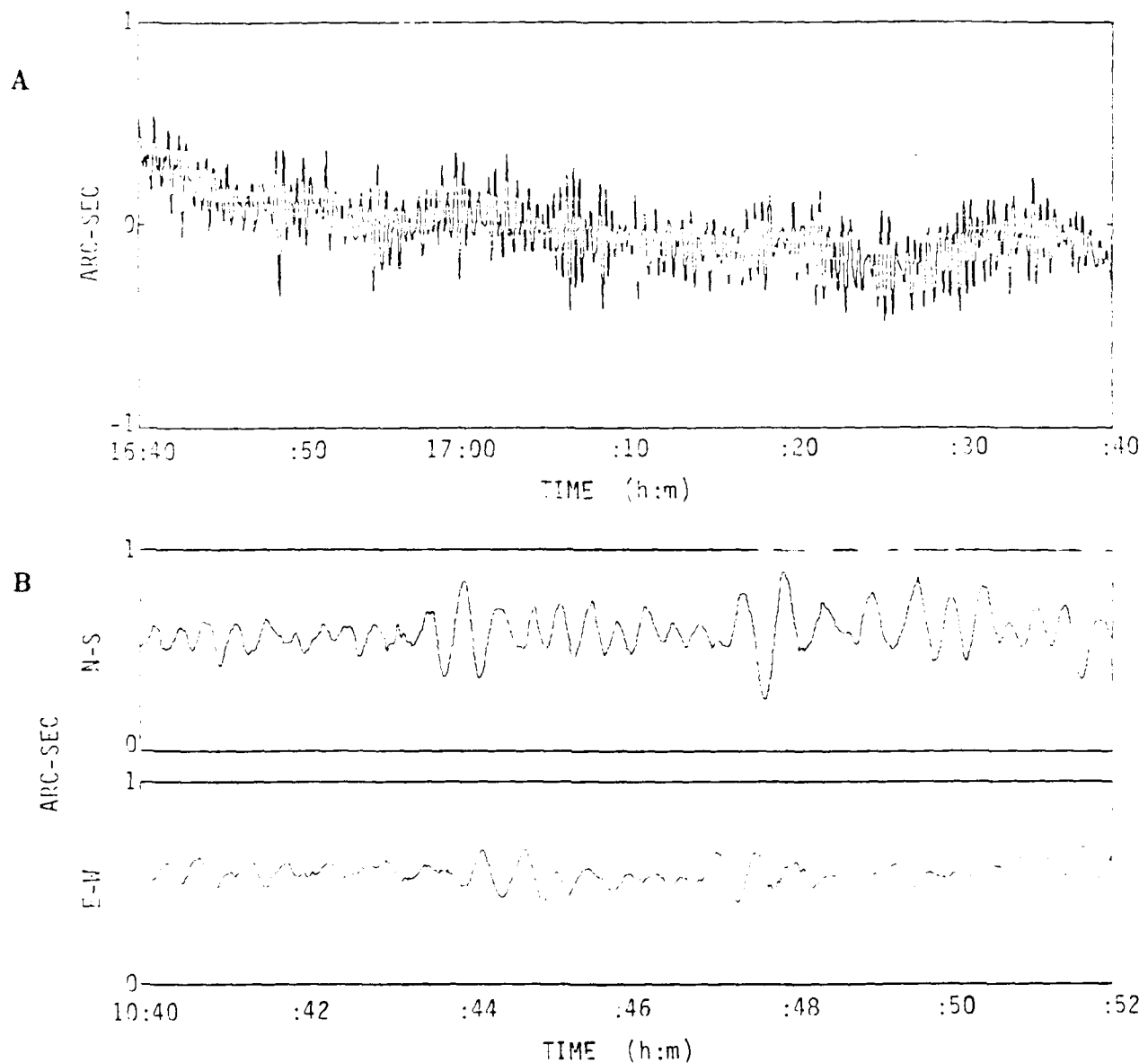
We calculate power spectra of representative records of tilt near the beginning, middle, and end of the experiment to study the natural tilt background in the eastern Arctic Ocean. Figure 3.7 shows the spectrum of tilt fluctuations in the north-south plane measured by tiltmeter 180, from file 089A, the first data record. Also shown is a spectrum of tilt recorded by the same instrument at the AIWEX camp on the Beaufort Sea in April 1985. The figure demonstrates the qualitative similarity of spectra recorded at widely separated points on the Arctic Ocean. Spectra show a broad peak centered at periods of 20 to 45 seconds and a steep rise in energy at frequencies below about 1 mHz. These features are separated by a spectral valley or window.

The spectral peak reveals flexural waves in the ice that represent swell from the open ocean propagating into the Arctic as flexural-gravity waves [Wadhams, 1986, and references therein]. Scattering at the ice edge effectively damps high frequency swell, allowing only low frequencies to reach the central pack ice. Plastic creep dissipates swell energy within the pack, attenuating shorter wavelengths more strongly than longer. The ice effectively acts as a lowpass filter, whose cutoff frequency decreases with increasing distance from the open ocean. The spectra of Figure 3.7 show that swell measured at the CEAREX O-camp, which was only a few hundred km from the open ocean, is stronger at short periods than swell measured at the AIWEX camp which was about 1000 km from the Bering Strait. The agreement between the spectra below the respective ice cutoff frequencies, from about 10 to 25 mHz, suggests that the tiltmeter measures the extreme low-frequency end of an infra-swell spectrum that may have a consistent form in the Arctic Ocean. Energy at frequencies between 20 and 40 mHz is about a factor of 3 higher than shown by long-period wave measurements off the California coastline [W. Munk, personal communication]. No physical model of long-period swell [Munk, 1962] predicts the energies observed by the tiltmeters in the Arctic. It is intriguing to speculate that



**FIGURE 3.5**

One example of time series from each tiltmeter, digitally lowpass filtered with a cutoff frequency of 10 mHz, displaying internal wave-like fluctuations. Vertical scales are in seconds of arc, and horizontal scales are hours UT. Internal wave tilts are typically several tenths of an arc-sec in amplitude; the record from file 107B shows a large soliton-like packet producing tilts of a few arc-sec amplitude.

**FIGURE 3.6**

Samples of time series showing fluctuations from flexural-gravity waves caused by long-period swell. (A) Tiltmeter 179, April 18, north-south tilt, displayed at 5 minutes per division (abscissa). (B) Tiltmeter 179, April 19, displayed at 1 minute per division (abscissa).

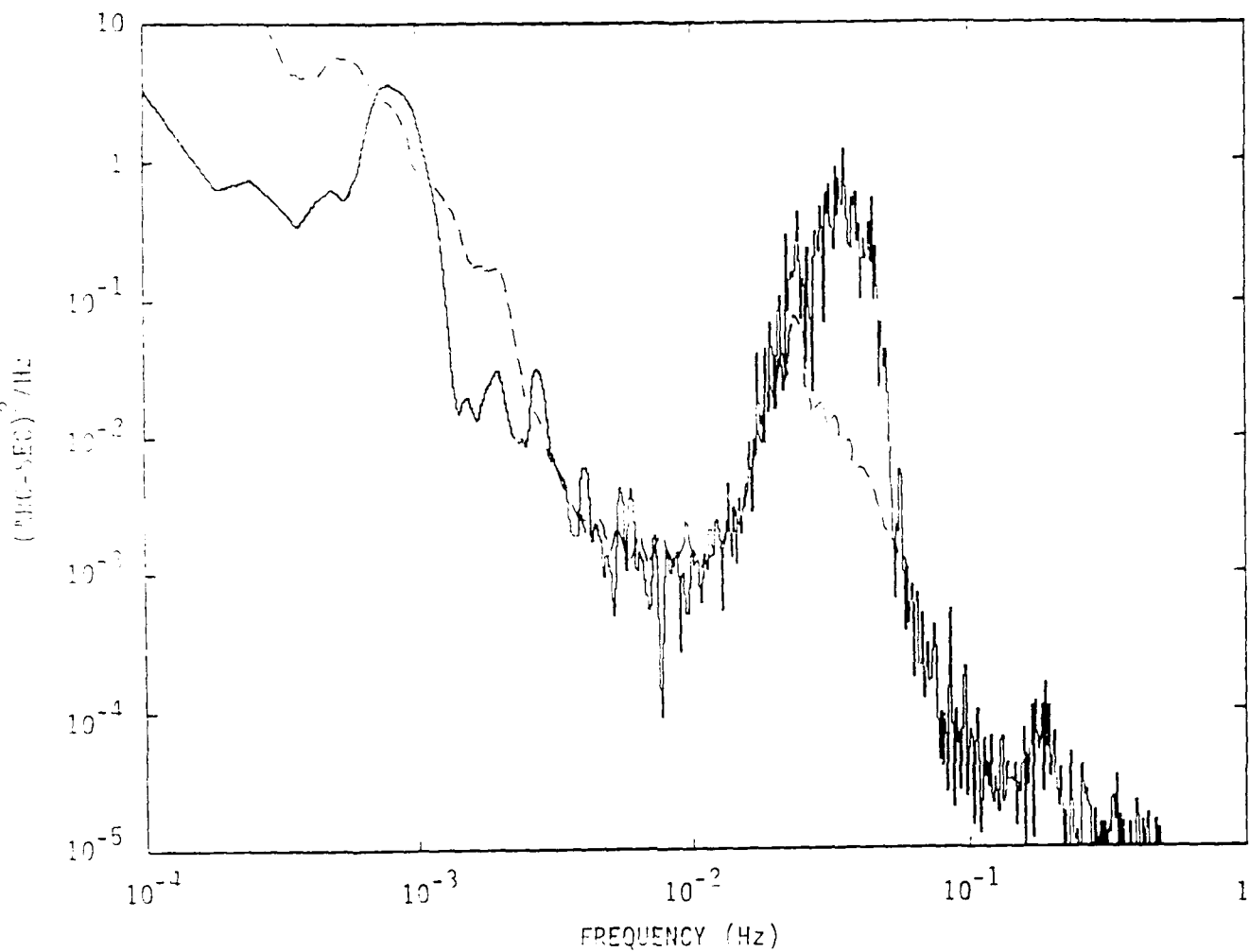


**FIGURE 3.7**

Spectrum of tilt fluctuations in the north-south plane measured by tiltmeter 180 during CEAREX (solid trace) and during AIWEX (dashed trace). CEAREX measurement was made at about  $83^\circ 3' \text{ N}$ ,  $9^\circ 53' \text{ E}$  on the night of 30–31 March 1989. AIWEX measurement was made at about  $73^\circ 59' \text{ N}$ ,  $145^\circ 15.5' \text{ W}$  on the night of 18–19 March 1985. Spectra show a rise in energy at frequencies below 2 mHz, and a spectral peak between about 20 and 50 mHz. Long-period swell at AIWEX is filtered more heavily because the ice edge was further away.

the same mechanism responsible for diminished internal wave energy in the Arctic also causes the increased infra-swell energy. In section 3.5, we show that tilts measured during CEAREX indicate that long-period swell comes predominantly from Fram Strait and the Greenland Sea.

The rise in tilt energy at low frequencies corresponds to internal wave-induced motion of the ice. The peak in the CEAREX spectrum at 3.25 cycles per hour (cph) agrees with the estimate of the highest buoyancy frequency at that time during CEAREX [J. Morison, personal communication]. Conclusions drawn on-site from oceanographic measurements show that internal wave activity and oceanic structure were highly variable during CEAREX [personal communications with T. Dillon, M. Levine, M. McPhee, J. Morison, L. Padman, C. Paulson]. For example, the thickness of the mixed layer varied from a minimum of 50 m to a maximum of about 150 m. This suggests that the internal wave portion of the tilt spectra should vary significantly from day to day. The unexpectedly large depth of the pycnocline means that internal wave generation by ice keels (and possible consequent ice-coupled waves) should be weak [CEAREX Situation Report No. 31, 1989].

**Figure 3.8** compares tilt spectra measured by tiltmeter 179 from three different records, day 89 (30 March) at the start of the experiment, day 99 (9 April) near the middle, and day 108 (18 April) near the end. It corroborates the expectation of variable internal wave activity and fairly consistent swell. Events generating broadband noise, discussed further in Section 3.6, fill in the spectral window on day 108.

**Figure 3.9** presents spectra as a function of time during day 99 as a waterfall plot. The swell peak is rather consistent from day to day or hour to hour; however, there is some variability both in the internal wave spectrum and in the noise level in the spectral window. The waterfall plot shows internal waves near the buoyancy frequency, about 3 cph, changing direction and magnitude during the day. In the middle of the record, the heading is more along the north-south axis than the east-west; later, the direction appears to rotate as the total amplitude diminishes. Noise level in the spectral valley appears to correlate with noise at frequencies higher than the swell peak. Examination of some records shows signals indicative of sudden events in the ice such as cracking or ridging. Ice cracks, discussed in section 3.6, show a spiky character that adds white noise to the spectrum, raising the floor of the valley.

### 3.4 Tilt amplitude anomaly

**Figure 3.10** shows spectra of simultaneous records of north-south tilt measured by each tiltmeter. Spectra are calibrated using the manufacturers' constants given in Table 1. The spectra do not overlay one another as expected. They indicate a difference in response magnitude across the entire measurement bandwidth. Examination of other records manifests the difference consistently. Tiltmeter AGI measures fluctuations about twice as large as tiltmeter 179, which in turn responds more than twice as strongly as tiltmeter 180.

Laboratory measurements show that relative calibrations between tiltmeters agree with manufacturers' specifications. The result represents either an instrumental effect or a physical inhomogeneity of the ice response. To cite an example of the first possibility, all three tiltmeters preamplify electrical signals using circuits at the sensor, exposed to ambient temperature. It is conceivable that the amplifier gains are considerably different below  $-20^{\circ}\text{C}$  than at  $+20^{\circ}\text{C}$ . Nevertheless, the tiltmeters are rated for operation to  $-35^{\circ}\text{C}$ , and gain control resistors are stable to several percent over the temperature range.

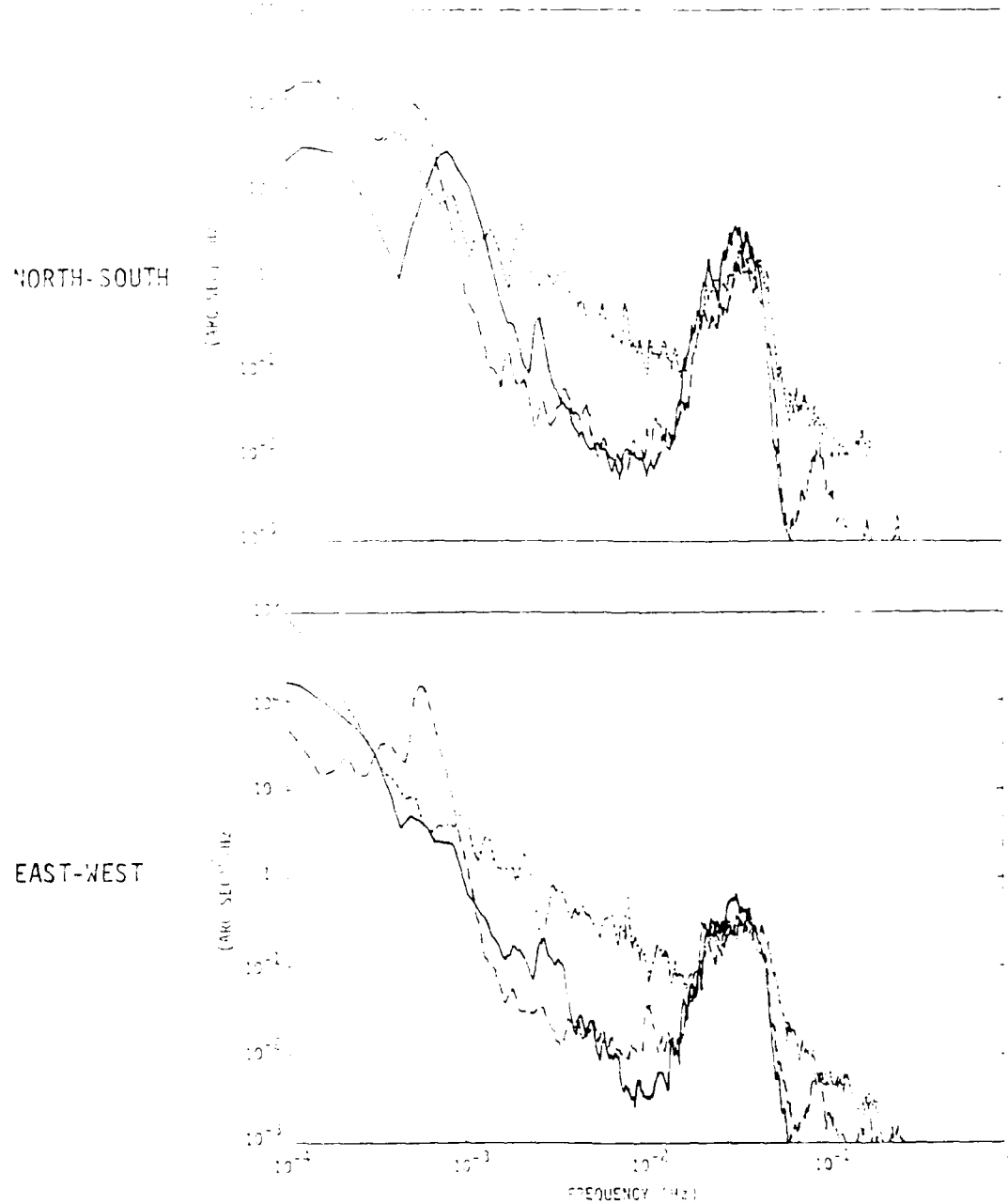


**FIGURE 3.8**

Spectra of tilt fluctuations in the north-south plane (top) and the east-west plane from 9.1 hour ( $2^{15}$  second) records of tiltmeter 179 on different days. Solid traces show measurements from file 089A; long-dashed traces show measurements from file 099A; and short-dashed traces show measurements from file 108A. Ice rupture events, discussed in section 3.6, add white noise to record 108A, filling in the spectral valley.

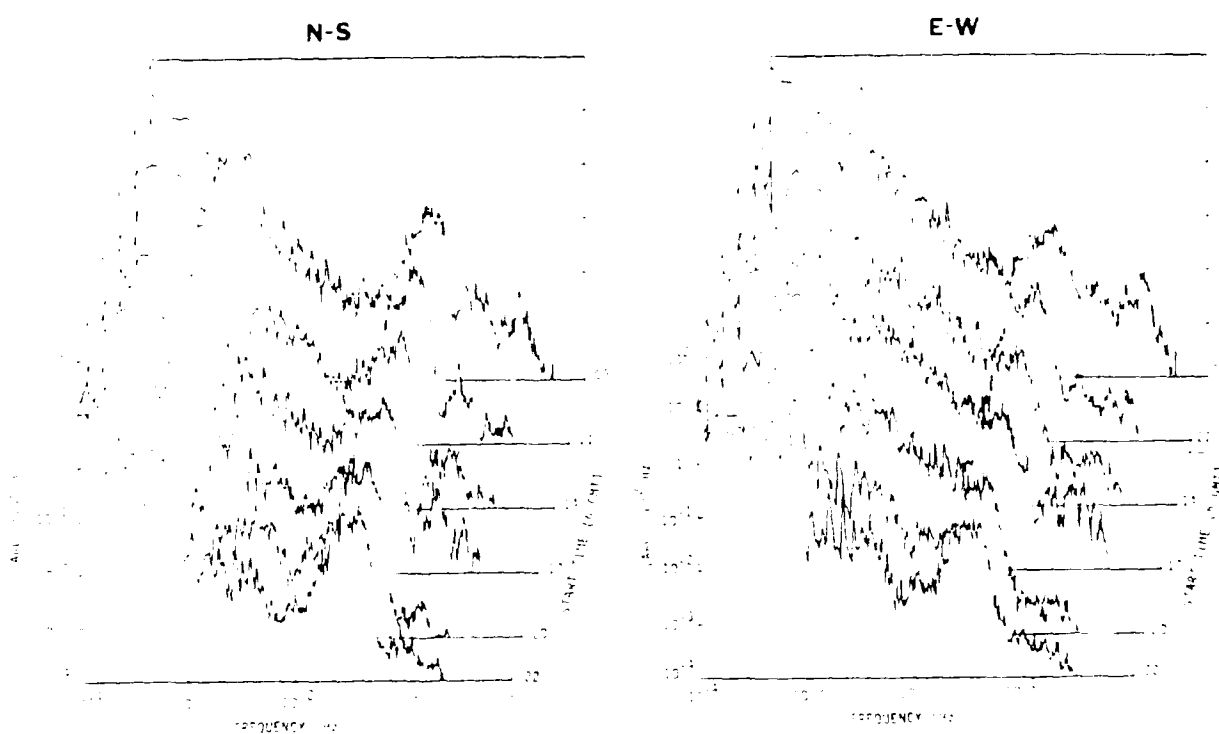


**FIGURE 3.9**

Waterfall plot of north-south (left) and east-west tilt fluctuation spectra measured by tiltmeter 180 during April 9. Each spectrum results from a 9.1 hour time series starting at the time indicated. Adjacent spectra overlap and show the time evolution of spectral signal characteristics during a one-day record. The spectral peak near the Brunt-Väisälä frequency of 3-4 cph shifts from one direction to the other during the day, showing the passage of internal waves travelling in different directions. Noise in the spectral valley varies as a function of ice rupture or ridging activity discussed in section 3.6.

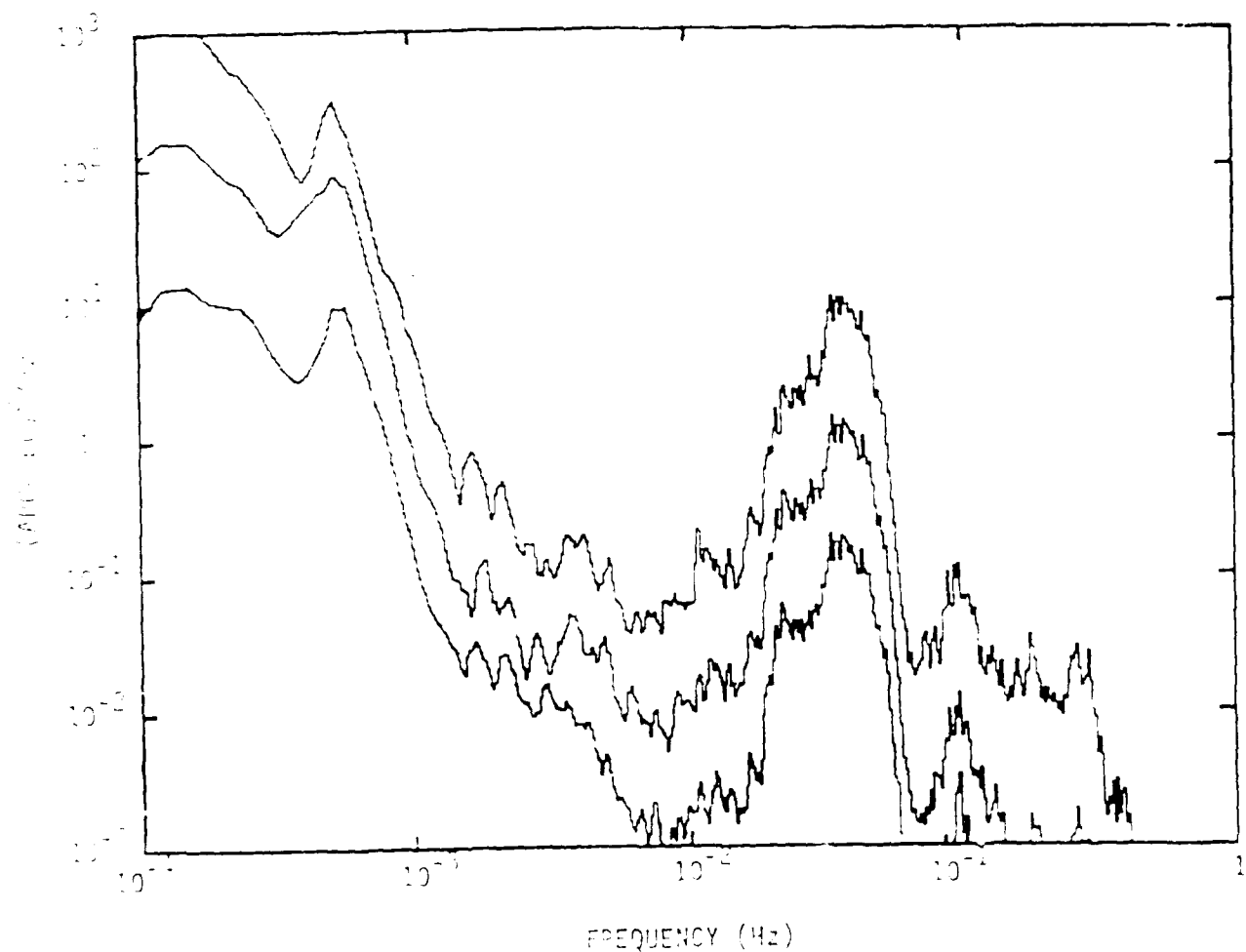


FIGURE 3.10

Power spectra of north-south tilt from simultaneous time series recorded on April 2 by each tiltmeter in the array, all plotted to the same scale indicated by the ordinate. Top trace, tiltmeter AGI; center trace, tiltmeter 179; bottom trace, tiltmeter 180. Spectra have been calibrated using the manufacturers' values listed in Table 1. Tiltmeter responses differ consistently over the frequency bandwidth by a factor between two and four in power. Spatial variations in ice thickness may distort ice response and explain the discrepancy, as discussed in Section 3.4.

Hence, factors of two in gain are difficult to explain as instrumental effects.

This leaves spatial variations in ice response in the region of the array as an alternative explanation. Most treatments of wave propagation on an ice-covered sea ignore the contribution of ice rigidity in the regime where wavelength much exceeds ice thickness [Wadhams, 1986]. The ice follows the liquid free surface displacement. This model implies that tilt response should be identical everywhere on the ice.

Alternative models can, however, suggest effects leading to spatial variations of ice tilt response. One alternative notes that propagating waves are accompanied by oscillating horizontal currents. Ice keels acting as sails catch the currents and experience a resulting torque. That torque can bend the ice and distort its response from that of the free surface. Another suggests that rigid, bottom-heavy ice near a ridge might heave up and down in response to wave-induced sea height displacements, with little tilting; thinner ice nearby then tilts more than the equivalent free surface to compensate. In either case, the response distortion at a given location depends on the surrounding keel distribution as well as on the ambient wave field. Whether such effects can dominate the response sufficiently to account for 100% variations in magnitude is a question for further study.

### 3.5 Directional spectra and array coherences

We examine a section of data 9.1 hours long and starting at 1989:099:11:00:00 by evaluating cross spectral coherence and transfer function (magnitude and phase) between different sensor time series. By examining cross spectra between parallel tilt axes on separate tiltmeters, we can determine the group velocity of waves propagating through the array. Cross spectra between different axes on the same tiltmeter give a separate measure of heading. The two provide a consistency check. In each case, the analysis is complicated if, at a given wavenumber, more than one wavevector is present. We present a way to tell if this is so.

#### 3.5.1 Phase between orthogonal tilt axes

Vertical displacement  $\zeta$  caused by a plane monochromatic wave of unit amplitude can be written

$$\zeta(\vec{r}, t) = e^{i(\vec{k} \cdot \vec{r} - \omega t + \varphi)}, \quad (3.1a)$$

where  $\vec{r}$  is position,  $\vec{k}$  is the wavevector,  $\omega$  is the frequency, and  $\varphi$  is the wave's phase. Tilt produced by the wave,  $\dot{\theta}$ , is the gradient of displacement, namely

$$\dot{\theta} = \vec{\nabla} \zeta. \quad (3.1b)$$

The expressions

$$\theta_x = \dot{x} \cdot \dot{\theta} = i(\vec{k} \cdot \dot{x})e^{i(\vec{k} \cdot \vec{r} - \omega t + \varphi)} \quad (3.1c)$$

and

$$\theta_y = \dot{y} \cdot \dot{\theta} = i(\vec{k} \cdot \dot{y})e^{i(\vec{k} \cdot \vec{r}_m - \omega t + \varphi)} \quad (3.1d)$$

respectively give x- and y-components of tilt,  $\theta_x$  and  $\theta_y$ . Equations 3.1c and 3.1d say that the two tilt axes are either in phase with each other or 180 degrees out of phase with each other, depending on the signs of the two projections of  $\vec{k}$ .

Now consider two incident waves at the same frequency, with amplitudes  $A_1$  and  $A_2$ , wavevectors  $\vec{k}_1$  and  $\vec{k}_2$ , and phases  $\varphi_1$  and  $\varphi_2$ . Since the waves share the same frequency  $\omega$ ,  $|\vec{k}_1| = |\vec{k}_2|$  and only the vector orientations differ. (Since the dispersion relation for flexural-gravity waves depends only weakly on ice thickness, it can be taken as independent of wave heading and invariant in space.) The wavevectors can be characterized by a single wavenumber,  $k$ , and two wave headings,  $\psi_1$  and  $\psi_2$ , which represent the angle between the wave heading and the x-axis of a coordinate basis. We normalize by  $A_1$  and choose our basis such that  $\vec{k}_1 \cdot \vec{r} = 0$ , without loss of generality. Choosing the time origin such that  $\varphi_1 = 0$ , and defining  $\varphi \equiv \vec{k}_2 \cdot \vec{r} + \varphi_2$ , we obtain the phase of the tilt components as

$$\phi(\theta_x) = \tan^{-1} \left( \frac{A \cos \psi_2 \sin \varphi}{\cos \psi_1 + A \cos \psi_2 \cos \varphi} \right) \quad (3.2a)$$

and

$$\phi(\theta_y) = \tan^{-1} \left( \frac{A \sin \psi_2 \sin \varphi}{\sin \psi_1 + A \sin \psi_2 \cos \varphi} \right). \quad (3.2b)$$

The phase between the two axes is the difference  $\phi(\theta_x) - \phi(\theta_y)$ , and in general it is nonzero. It is also nonzero in general for superpositions of any number of waves at a given frequency.

This relation provides a means of determining whether waves impinging on the tiltmeter come from a single source or are a superposition of waves from several sources. If the phase between two orthogonal tilt axes at a given frequency is either 0 or  $180^\circ$ , then waves at that frequency most likely come from a single direction. Any other phase guarantees that the oscillation is a superposition of waves from different directions.

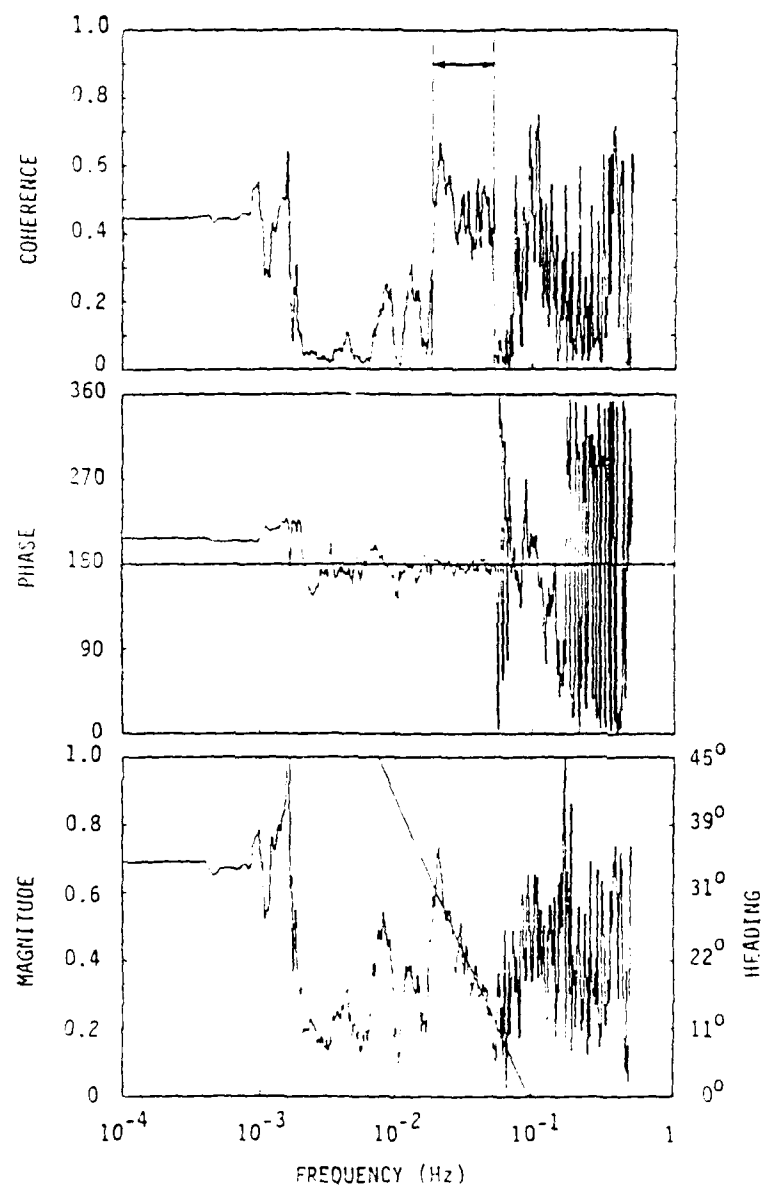
### 3.5.2 Wave heading determined using a single biaxial tiltmeter

Once waves have been shown to come from a single direction by the analysis above, that direction can be determined with one biaxial tiltmeter. The magnitude transfer function relating the two axes gives the heading,  $\psi$ , according to the relation

$$\psi = \tan^{-1} \left( \frac{k_y}{k_x} \right) = \tan^{-1} \left( \frac{|\theta_y|}{|\theta_x|} \right). \quad (3.3)$$

Results of cross spectral analysis of a 9.1 hour record of the x-axis and y-axis of tiltmeter 179 starting on 1989:09:11:00:00 are shown in Figure 3.11. Coherence between the two tilt axes is high in the swell band between about 20 mHz and 50 mHz. The phase is zero in the band, indicating that the swell is dominated by a single origin at each frequency. The magnitude transfer function shows a monotonic variation in the swell band, meaning that direction of the swell depends on frequency. Analysis of the other two tiltmeters yields similar results.

Figure 3.12 shows a map of the Arctic around Svalbard, indicating the approximate position of the O-camp. Lines emanating from the camp site bound the range of swell headings indicated by the analysis of each tiltmeter record. It shows that swell is

**FIGURE 3.11**

Cross spectra between orthogonal tilts measured by tiltmeter 179 during a record 2<sup>15</sup> seconds long from file 099A. Spectra have been averaged over 33 points or a bandwidth of 1 mHz. Top trace shows the squared coherence between axes; the long-period swell band between 20 and 50 mHz, where coherence is consistently high, is identified. Center trace shows the phase between axes; it is 180° in the swell band. The magnitude transfer function shown in the bottom trace plots the ratio of east-west tilts to north-south tilts as a function of frequency. The left-hand ordinate displays relative magnitude, which is converted to swell heading in the right-hand ordinate.

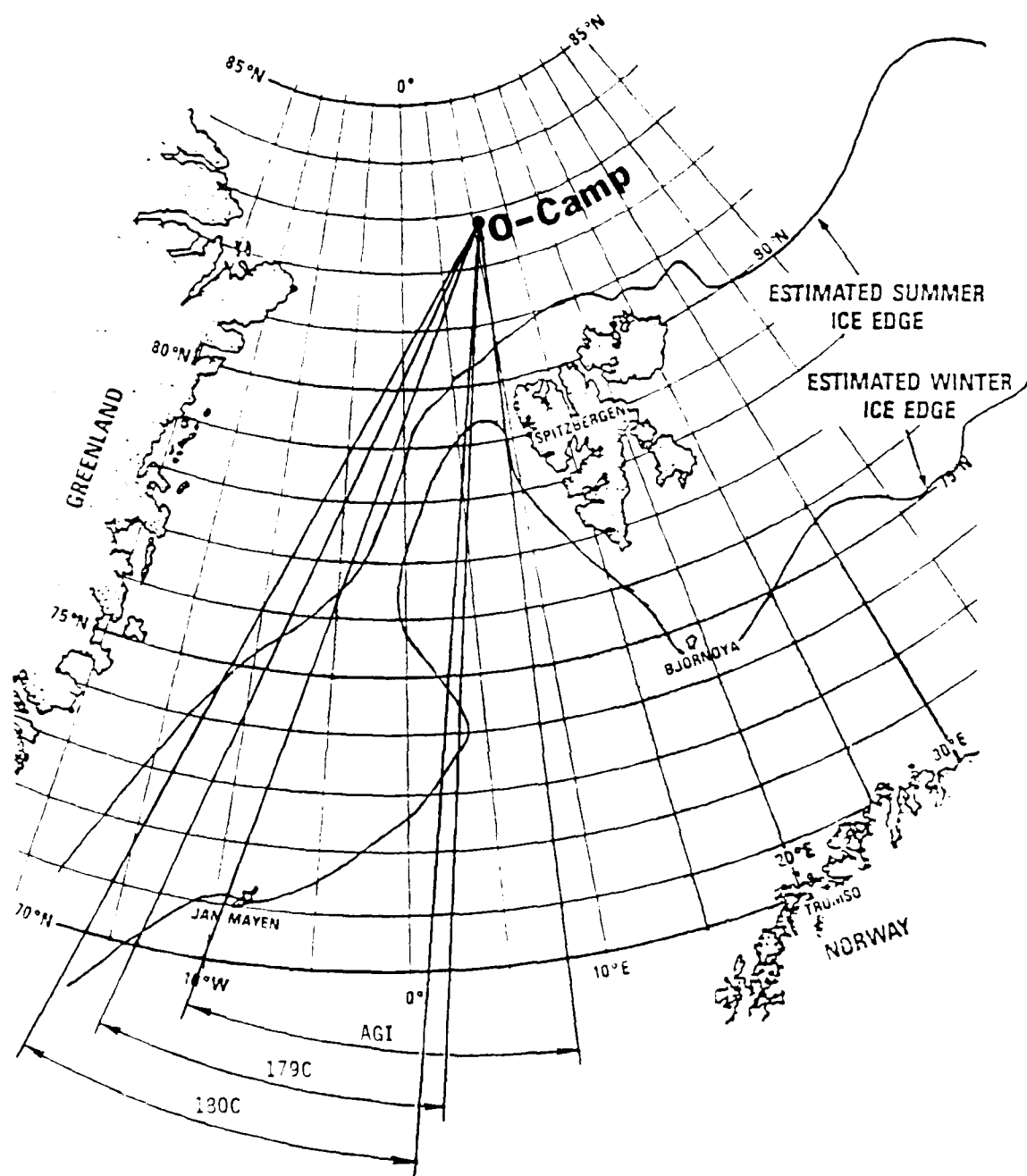


**FIGURE 3.12**

The range of headings of swell impinging on the tiltmeter array, determined by cross spectral analysis of orthogonal tilt axes. Headings were determined using each tiltmeter separately. High-frequency components (near 50 mHz) come predominantly from the eastern Fram Strait, where they pass through less ice, as indicated by ice edge estimates; low-frequency components (near 20 mHz) are less attenuated and come from the western Fram Strait.

dominated by the contribution of the north Atlantic coming through Fram Strait.

Low frequency swell comes from the western edge of the Fram Strait, and high frequency swell from the eastern edge. Swell from the western edge, passing the Greenland coast, travels through sea ice for a greater distance than swell from the eastern part, as indicated by average sea ice boundaries on the map. High frequency swell from the western region is more heavily attenuated than swell from the east, explaining the dependence of heading on frequency.

Note that phase between tiltmeter axes in the internal wave band is nonzero, indicating a superposition of modes propagating in different directions. Thus, a simple analysis of two orthogonal tilt axes cannot reveal predominant headings of internal waves during this period. Examination of tiltmeter time series from April 17, plotted in Figure 3.13, shows how this can be the case. The large internal wave packet near the center of the record (labelled A in the Figure) shows up strongly on the north-south tilt axis and only weakly on the east-west axis. The two signals are in phase; the relative magnitudes correspond to a wave heading of about  $+15^\circ$  from north. The smaller wave train after the large packet (labelled B) shows up about equally on both axes, which furthermore are  $180^\circ$  out of phase with each other, implying a heading of about  $-45^\circ$ . In other words, wave heading changes with time. Spectral analysis, which averages the ensemble, yields a phase between 0 and  $180$  degrees, indicating waves propagating in more than one direction. A simple cross spectral analysis cannot distinguish between several headings present simultaneously or occurring in succession, as is the case during file 107B. This shows that a detailed analysis of internal wave induced tilt and strain fluctuations must be approached with care.

### 3.5.3 Heading and group speed determined using a tiltmeter array

The analysis described above, using the orthogonal axes of a single tiltmeter, can determine the propagation direction of a single-mode wave. It cannot determine the dispersion relation or the wave group or phase speed. An array of instruments can yield all these quantities. Consider an array of three sensors illustrated in Figure 3.14. The phase lag of a signal between sensor  $i$  and sensor  $j$ ,  $\varphi_{ij}$ , is given by  $\varphi_{ij} = \vec{k} \cdot \vec{r}_{ij}$ , where  $\vec{r}_{ij}$  is the vector from position  $i$  to position  $j$ . A wave with  $\vec{k} \equiv k \cos\psi \hat{x} + k \sin\psi \hat{y}$ , where  $\hat{x}$  points from sensor 1 to sensor 2, produces phase shifts around the array given by

$$\varphi_{12} = k r_{12} \cos\psi, \quad (3.4a)$$

$$\varphi_{13} = k r_{13} \cos(\Phi - \psi), \quad (3.4b)$$

and

$$\varphi_{23} = \varphi_{13} - \varphi_{12}, \quad (3.4c)$$

where  $r_{ij} \equiv |\vec{r}_{ij}|$  and  $\Phi$  is the angle of the triangle vertex at sensor 1, as Figure 3.14 shows.

Differentiating equations 3.4a and 3.4b with respect to frequency  $\omega$  and using the expression for group velocity,  $c_g = d\omega/dk$ , we find:

$$\psi = \tan^{-1} \left( \frac{1}{\sin\Phi} \left[ \frac{\varphi'_{13}}{r_{13}} - \frac{\varphi'_{12}}{r_{12}} \right] \right) \quad (3.5a)$$

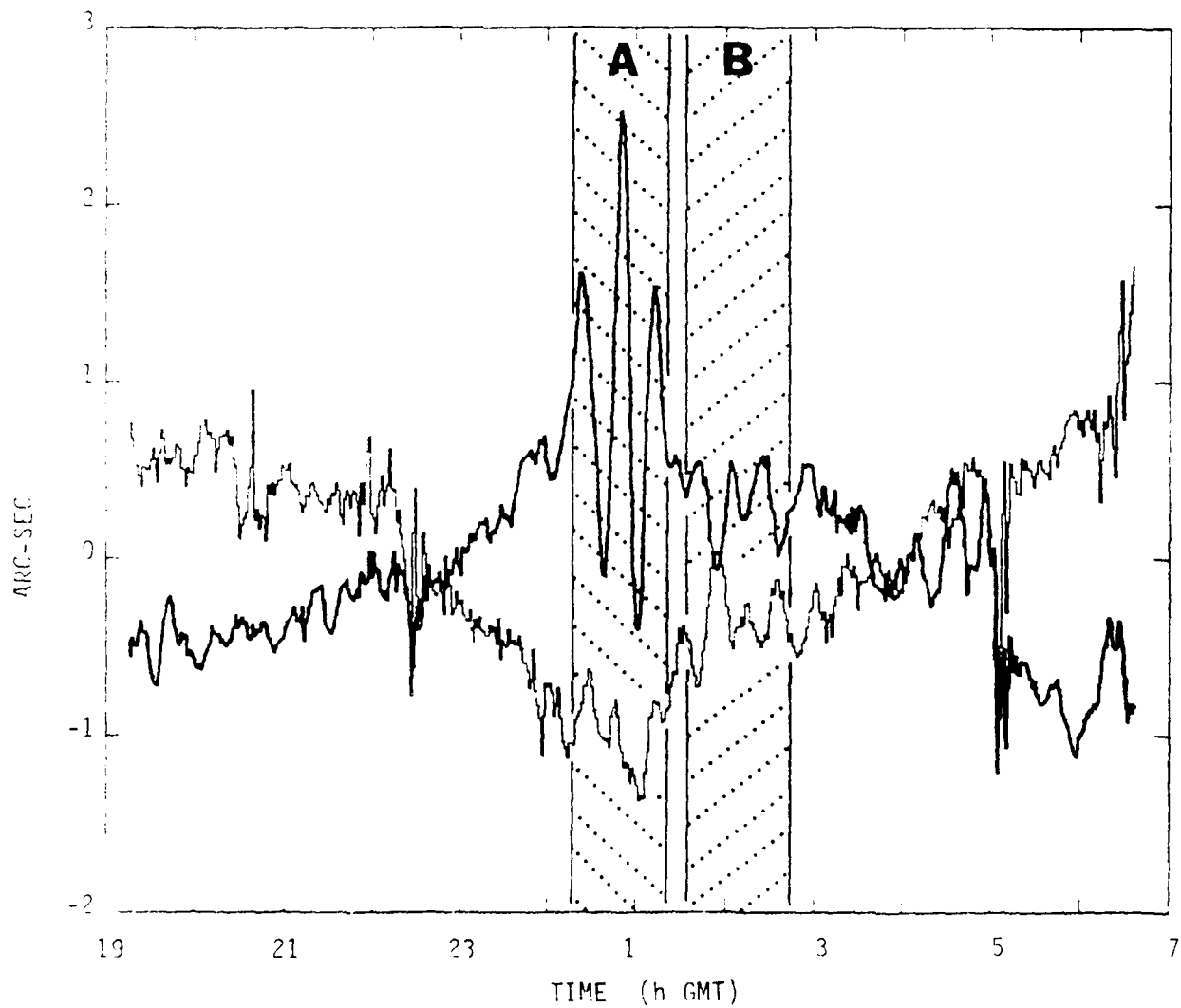


**FIGURE 3.13**

North-south (heavy trace) and east-west tilt fluctuations from file 107B, measured by tiltmeter 180. The stippled region labelled A highlights a strong internal wave packet causing tilts predominantly in the north-south plane. A smaller amplitude packet immediately following, labelled B, produces tilts of about equal magnitude on both axes, indicating a different propagation direction.

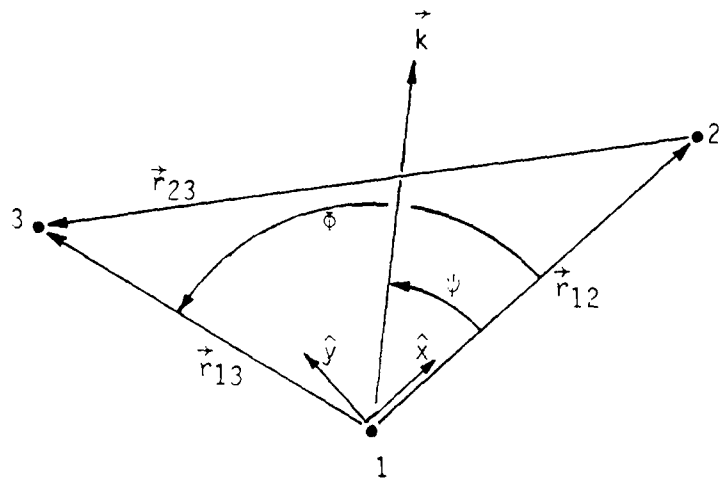


**FIGURE 3.14**

Definition of terms for analysis of signals propagating with wavevector  $\vec{k}$  through an arbitrary triangular array of sensors 1, 2, and 3.

and

$$c_g = \frac{\varphi'_{12}}{r_{12} \cos \psi}, \quad (3.5b)$$

giving heading and the dispersion relation governing wave propagation.

The above analysis can be used with any scalar sensor of wave motion in an array. In our particular case, we can obtain wave heading and dispersion relations using either projection of tilt,  $\theta_x$  or  $\theta_y$ , around the array. Results should be independent of the axis chosen except in the special case when wave propagation is aligned with one axis, producing no measurable signal in the other. (In such a case, the poor coherence between tiltmeter axes warns us not to proceed heedlessly.)

The spectral analysis described above averages propagation information over the entire time series. Individual wave packets in the record can be analyzed by an analogous procedure in the time domain, replacing  $\varphi_{ij}$  in equations 3.4 by  $\Delta t_{ij}/T$ , where  $\Delta t_{ij}$  is the time delay between sensors  $i$  and  $j$ , and  $T$  is the dominant period of the packet:

$$\psi = \tan^{-1} \left( \frac{1}{\sin \Phi} \left[ \frac{r_{12}}{r_{13}} \frac{\Delta t_{13}}{\Delta t_{12}} - \cos \Phi \right] \right) \quad (3.6a)$$

and

$$\lambda = \frac{T r_{12} \cos \psi}{\Delta t_{12}}. \quad (3.6b)$$

### 3.5.3.1 Long-period swell through the array

We analyze the same set of records as in Section 3.5.2. Figure 3.15, the result of cross-spectral analysis, presents phases  $\varphi_{12}$ ,  $\varphi_{13}$ , and  $\varphi_{23}$  as a function of frequency for the north-south tilts of the array. Straight-line fits to phase in the swell frequency band yield the following expressions, where we identify sensor 1 with tiltmeter 179, sensor 2 with tiltmeter 180, and sensor 3 with tiltmeter AGI:

$$\varphi_{12} = \begin{cases} -1.88\omega + 0.26, & 0.13 \leq \omega \leq 0.19 \\ -3.84\omega + 0.63, & 0.19 \leq \omega \leq 0.31 \end{cases}, \quad (3.7a)$$

$$\varphi_{13} = \begin{cases} +0.69\omega + 0.04, & 0.13 \leq \omega \leq 0.19 \\ -1.67\omega + 0.49, & 0.19 \leq \omega \leq 0.31 \end{cases}, \quad (3.7b)$$

and

$$\varphi_{23} = +2.31\omega - 0.18, \quad 0.13 \leq \omega \leq 0.31. \quad (3.7c)$$

Here, phases  $\varphi_{ij}$  are given in radians. Slopes of the straight lines,  $\varphi'_{ij}$ , define a wave group according to equations 3.5a and 3.5b. Equations 3.7 tell us that we have two wave groups present in the swell band. We find that the first group, spanning frequencies from 20 to 30 mHz, travels on a heading of 46.4 degrees true, while the second group, spanning the interval from 30 to 50 mHz, propagates along a heading of 3.6 degrees true.

Group headings, shown in Figure 3.16, are consistent with headings determined using orthogonal axes of a single tiltmeter and shown in Figure 3.12. We compare measured group speeds to those predicted by the free surface gravity wave dispersion relation,  $c_g = g/2\omega$  where  $g$  is the acceleration of the earth's gravity. Table 5 lists measured and predicted group speeds.

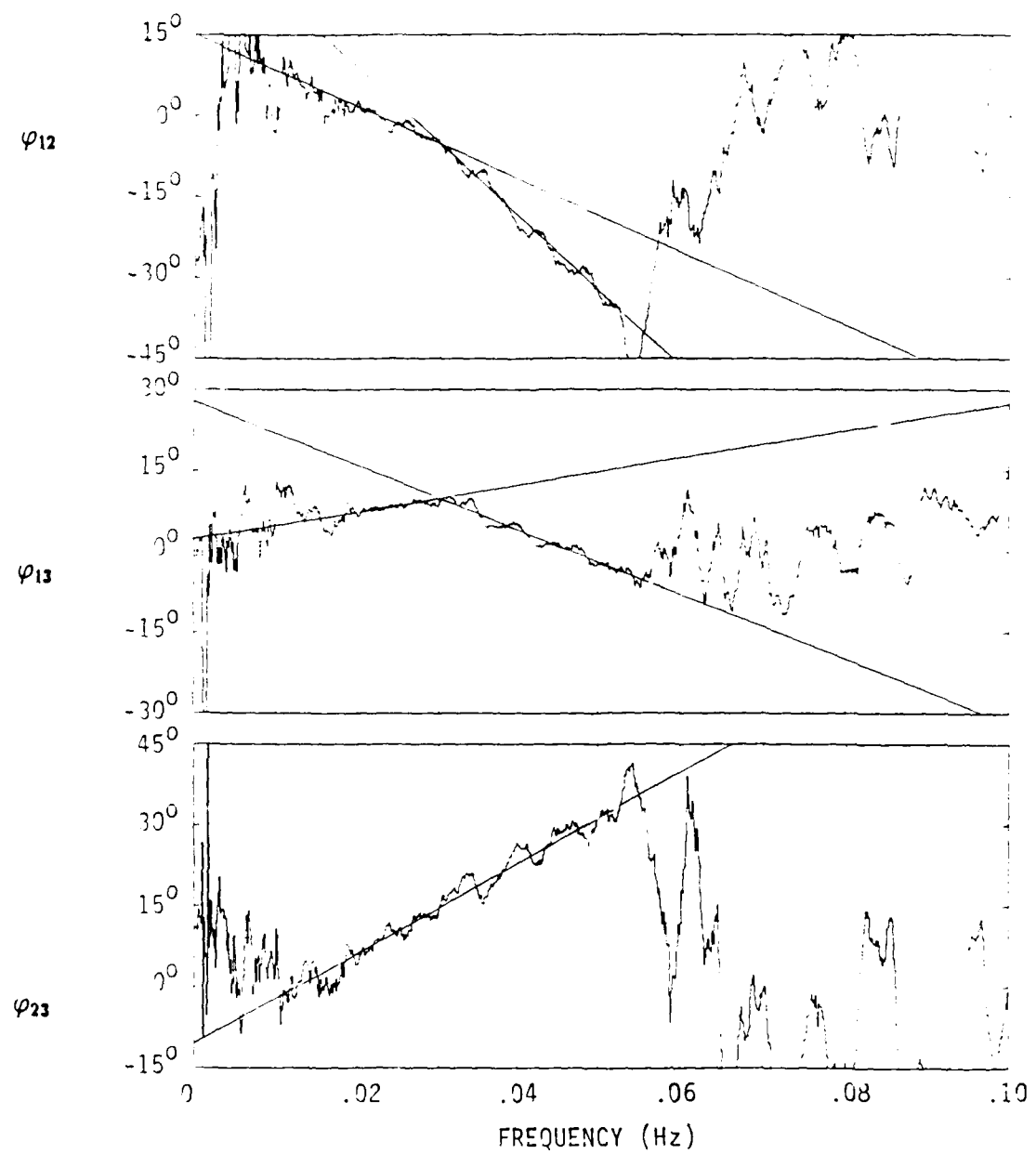


**FIGURE 3.15**

Phase differences generated by cross spectral analysis of north-south tilt fluctuations of the three tiltmeters for a 2<sup>15</sup> second record from file 099A. Phase plots result from 67-point spectral averages. Subscript 1 identifies tiltmeter 179; subscript 2, tiltmeter 180; and subscript 3, tiltmeter AGI. Straight lines represent linear fits that identify two distinct wave groups impinging on the array.

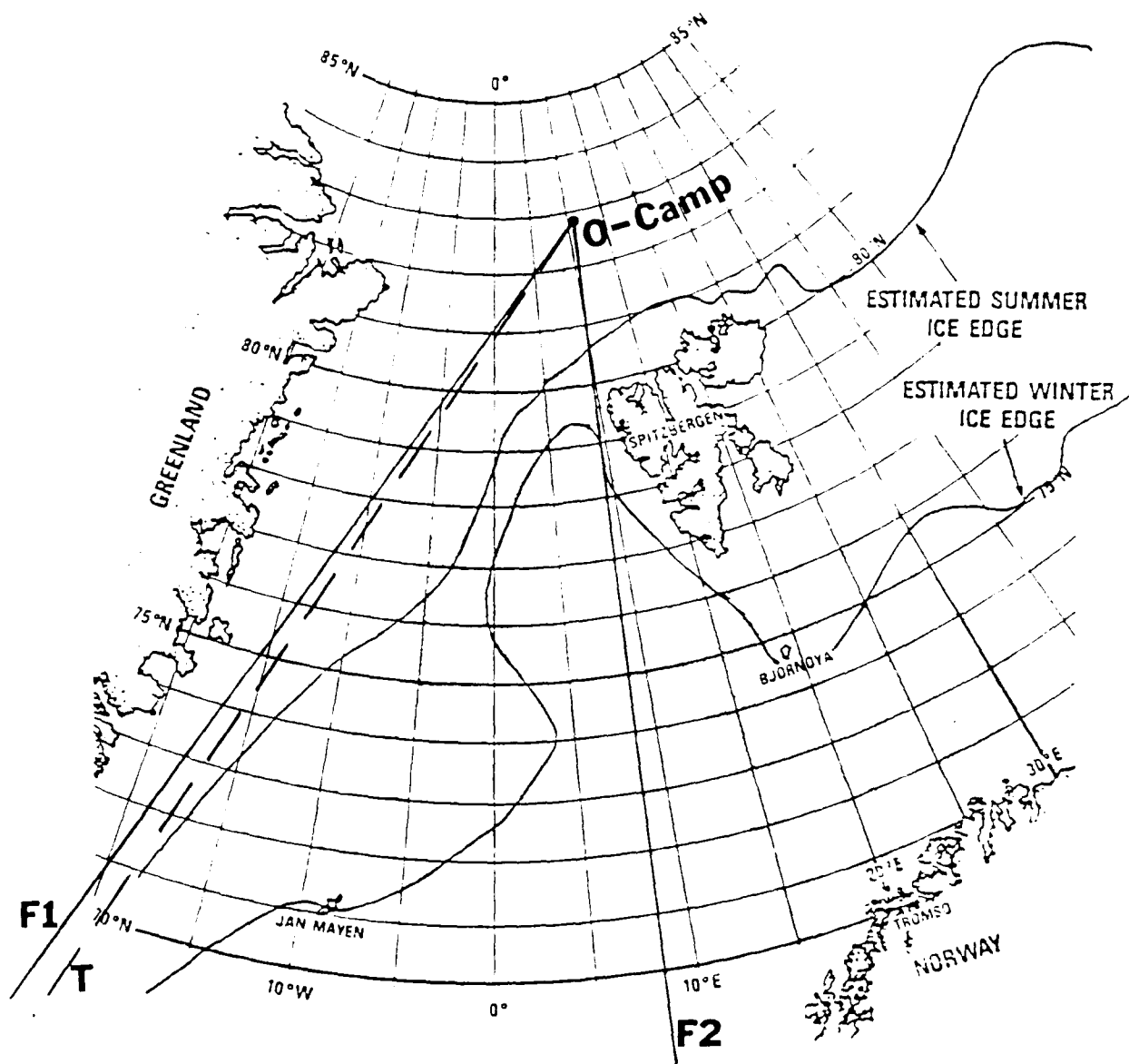


**FIGURE 3.16**

Map of the eastern Arctic showing the heading of the two wave groups reaching the O-camp, identified by cross-spectral analysis of phase. F1 marks the lower frequency group (center frequency 25 mHz), and F2 labels the higher frequency group (center frequency 40 mHz). Headings agree reasonably well with those derived by analysis of individual tiltmeters. Dashed line identified by T shows heading of an individual wave packet analyzed by the time domain method.

**TABLE 5.**  
*LONG-PERIOD SWELL GROUP SPEEDS*

<u>FREQUENCY</u>	<u>MEASURED SPEED</u>	<u>PREDICTED SPEED</u>
25 mHz	47.2 m/sec	31.2 m/sec
40 mHz	18.7 m/sec	19.5 m/sec

The ice cover exerts little influence on the propagation of surface waves whose wavelength is much greater than the ice thickness, so results should agree well with the free surface gravity wave dispersion relation [Wadhams, 1986]. Indeed, measured and predicted group speed agree within 5% for the higher frequency group. However, the discrepancy is about 50% for the lower frequency group. The discrepancy remains unexplained at present, and represents a challenge for further study.

Figure 3.17 shows north-south tilts induced on the three tiltmeters by one wave packet traversing the array near the center of the record used for cross-spectral analyses above. The packet is nearly monochromatic over the two oscillations shown, with a frequency of 42 mHz. Measuring the time delays between tiltmeters at all peaks and zero crossings of the packet and using equations 3.6a and 3.6b, we find an average heading of  $44.8^\circ$  true and a wavelength of 1552 m. This yields a phase speed  $c_p \equiv \lambda f = 71$  m/sec. While the heading, shown on Figure 3.16, is consistent with results of other approaches, the wavelength and phase speed differ from the free surface gravity wave predictions by 59% and 82%, respectively. The reason for the discrepancy is, again, unknown.

### 3.5.3.2 Internal wave packet

Figure 3.18 shows the tilt fluctuations induced on the three tiltmeters by the largest internal wave signal in the data set. It arrives at the array shortly after midnight on 18 April, and lasts until about 01:30. The figure shows the north-south axis of tiltmeters 179 and 180, and the (nominally) east-west axis of tiltmeter AGI. (Its north-south axis had gone offscale one week earlier.) The  $13^\circ$  misalignment of tiltmeter AGI with respect to the other two means that the nominal east-west axis responds to north-south tilts with the attenuation factor  $\sin(13^\circ) = 0.225$ . The three axes shown in the Figure hence suffice to determine wave heading and speed according to equations 3.6a and 3.6b.

Measuring time lags of the wave packet around the array gives us a wave heading of  $21^\circ$  true. Figure 3.19 shows the internal wave heading, superimposed on a bathymetric chart of the Arctic Ocean. It shows that the packet arrives from the direction of the Yermak Plateau. The resemblance of the packet to a slightly dispersed delta function [M. Longuet-Higgins, personal communication] suggests that the packet originates relatively nearby, rather than coming from the Atlantic via Fram Strait that lies beyond the plateau. The distance from the array to the plateau edge (defined by the contour of 1000 m depth) is about 70 km, and to the plateau center, about 150 km.

The characteristic frequency of the packet is 0.73 mHz or 2.6 cph. Array lags give an estimate of wavelength, 615 m, and of phase speed, 0.44 m/sec. The dispersion relation for internal waves is

$$\omega^2 = gk \frac{\delta\rho}{\rho_0} \{ \coth(kd) + \coth[k(D-d)] \}^{-1} \quad (3.8a)$$

where  $d$  is depth to the thermocline,  $D$  is depth to the bottom, and  $\delta\rho/\rho_0$  is the

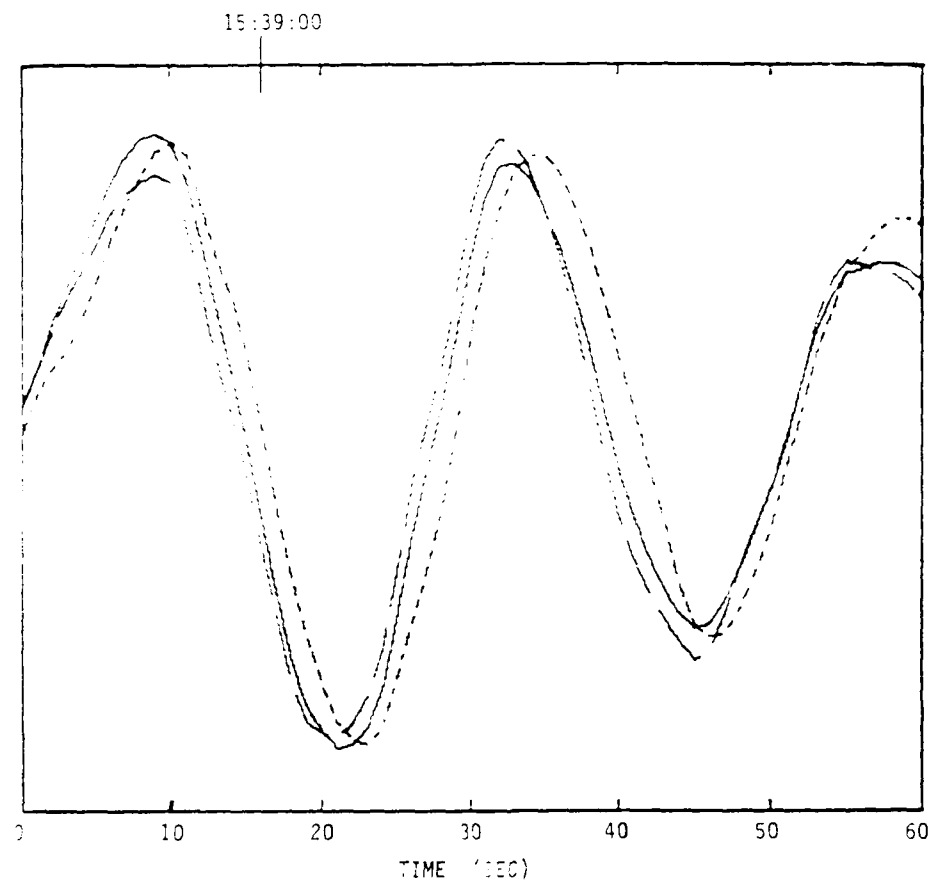


**FIGURE 3.17**

North-south tilt time series from tiltmeter 179 (solid trace), tiltmeter 180 (short dashes), and tiltmeter AG1 (long dashes). The record is excerpted from file 099A and represents a period around 15:39 hours on 9 April. The three signals have been scaled to match the amplitude for a better measurement of time lags.

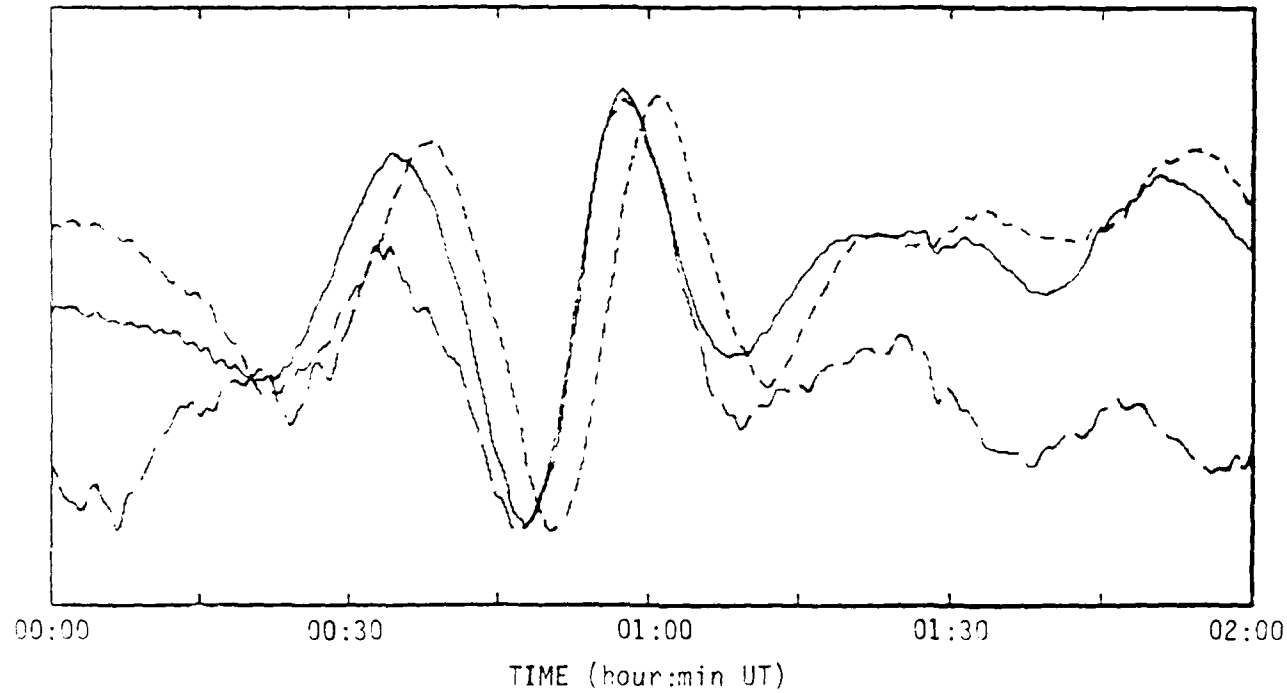


**FIGURE 3.18**

Time series of the north-south tilt axes of tiltmeter 179 (solid trace) and tiltmeter 180 (short dashes), as well as the nominally east-west axis of tiltmeter AGI, during passage of the strong internal wave packet at about 01:00 hours on 18 April. Signals have been scaled to match amplitudes for a better measurement of time lags. The raw output of tiltmeter 180, which is electronically inverted with respect to the other two, is here inverted again to show the proper phase. The discussion of section 3.5.2 shows that either orthogonal tilt axis suffices for phase measurements if the wave is unidirectional. Hence we use the east-west axis of tiltmeter AGI in place of its north-south axis which is offscale.

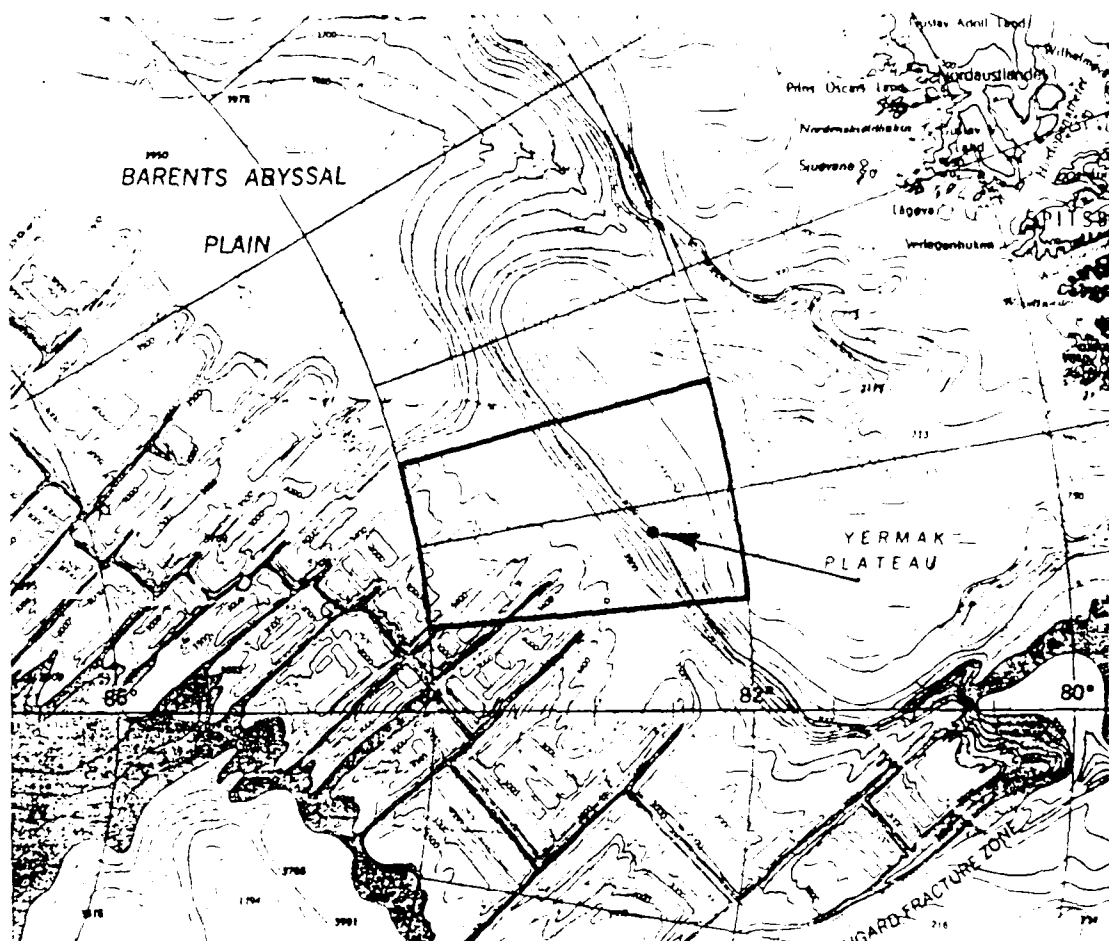


**FIGURE 3.19**

Bathymetric chart of the Arctic Ocean [American Geographical Society, 1975] showing the location of O-camp on 18 April and the heading of the internal wave packet shown in Figure 3.18. The heading,  $21^\circ$  true, places the packet's origin in line with the center of the Yermak Plateau as well as the Atlantic beyond Fram Strait.

fractional difference in water density above and below the thermocline [Phillips, 1980]. The camp was over about 3000 m of water on 18 April. Assuming a value of 100 m for  $d$ , about average for the highly variable conditions during CEAREX, and using the estimates of frequency and wavelength given above, we find a fractional density difference of about  $4.7 \times 10^{-4}$ , a reasonable value. Substituting this value into the expression for the Brunt-Väisälä frequency [*ibid.*],

$$N = \sqrt{-\frac{g}{\rho_0} \frac{\partial \rho}{\partial z}} \approx \sqrt{\frac{g}{d} \frac{\delta \rho}{\rho_0}}, \quad (3.8b)$$

we obtain an estimate  $N \approx 3.9$  cph, again a reasonable figure. The consistency of the estimates shows that the ice tilt fluctuation is indeed produced by an internal wave travelling past the array, northward from the direction of the Yermak Plateau.

### 3.6 Tilt, strain, and internal waves

Tilt measurements at AIWEX [Czippott and Podney, 1985] and CEAREX suggest that internal waves cause flexure of the ice by vertical displacement of the ocean surface. Strain measurements during *Fram 3* [Manley et al., 1982] suggest that internal waves may drive compressional waves in the ice cover as well. The apparent internal wave packet discussed in Section 3.5.3.2 provides an opportunity to look at flexure and compression from internal waves.

#### 3.6.1 Flexural and compressional waves in the ice

A monochromatic plane flexural wave of amplitude  $A$  and wavenumber  $k$  in a sheet of thickness  $h$  produces a sinusoidal vertical displacement,  $\zeta = A \sin kx$ . For small angles, the surface tilt  $\theta_x$  is just the derivative:  $\theta_x = d\zeta/dx$ . The strain component  $\epsilon_{xx}$  is given by

$$\epsilon_{xx} = -D \frac{d^2 \zeta}{dx^2}, \quad (3.9)$$

where  $D$ , the distance from the surface to the neutral bending line, is of the order of  $h/2$  [Sommerfeld, 1950]. The expression relating magnitude of tilt to magnitude of strain fluctuations for a flexural wave is

$$\epsilon_{xx} \approx (hk/2)\theta_x. \quad (3.10a)$$

On the other hand, we find the relation between tilt and strain for a monochromatic plane longitudinal (compressional) wave to be given by

$$\epsilon_{xx} \approx [2(1-\nu)/hk\nu]\theta_x, \quad (3.10b)$$

where  $\nu$  is Poisson's Ratio [Kolsky, 1963]. Doronin and Kheisin [1977] quote measurements in which  $\nu$  ranges between 0.3 and 0.44.

Equations 3.10a and 3.10b show that the wavenumber dependence of the tilt-strain relation differs markedly depending on whether the deformation is flexural or compressional. One consequence is that tiltmeters respond more sensitively to flexural waves and strainmeters to compressional waves; another is that by measuring both, we can ascertain whether a given wave is flexural, compressional, or a superposition of the two.

Spectral analysis techniques can be used to extend the method to the case of a distribution of waves over frequency and wavevector. Let the distribution of waves be described as the superposition of plane waves of vertical displacement amplitude  $A(\vec{k}, \omega)$ , where  $\vec{k}$  is the wavevector and  $\omega$  is the circular frequency:

$$\zeta(\vec{r}, t) = A(\vec{k}, \omega) e^{i(\omega t - \vec{k} \cdot \vec{r})} \quad (3.11)$$

The tilt about the  $x$  axis measured as a function of time  $t$  at position  $\vec{r} = (x, y, z)$  is given by the following integral over frequency and wavevector:

$$\theta_x(\vec{r}, t) = - \iint d\vec{k} d\omega i(\hat{x} \cdot \vec{k}) A(\vec{k}, \omega) e^{i(\omega t - \vec{k} \cdot \vec{r})}. \quad (3.12a)$$

For a flexural wave,  $\epsilon_{xx}$  is given by

$$\epsilon_{xx}(\vec{r}, t) \approx -(h/2) \iint d\vec{k} d\omega (\hat{x} \cdot \vec{k})^2 A(\vec{k}, \omega) e^{i(\omega t - \vec{k} \cdot \vec{r})} \quad (3.12b)$$

The cross spectrum between tilt and strain is given by

$$P_{\theta\epsilon}(\omega) \propto \int d\vec{k} (\hat{x} \cdot \vec{k}) (\hat{x} \cdot \vec{k})^2 P(\vec{k}, \omega) \quad (3.13)$$

where  $P(\vec{k}, \omega)$  is the power spectrum of wave vertical displacement; it can be expressed as

$$P(\vec{k}, \omega) = \Gamma(\vec{k}) \delta(\omega - \omega_0(k)). \quad (3.14)$$

Here, the delta function specifies frequency as a function of wavenumber according to the dispersion relation  $\omega_0(k)$ , and  $\Gamma(\vec{k})$  gives the power as a function of wavevector, or equivalently, wavenumber and wave heading,  $\psi$ :  $\Gamma(\vec{k}) \equiv \Gamma(k, \psi)$ . We can rewrite the cross spectrum as

$$P_{\theta\epsilon}(\omega) \propto \iint k dk d\psi (\hat{x} \cdot \vec{k})^3 \Gamma(k, \psi) \delta(\omega - \omega_0(k)). \quad (3.15)$$

If the wave distribution is isotropic, then  $\Gamma(k, \psi)$  is a function of  $k$  alone, and we can separate the  $k$  and  $\psi$  integrals. The latter is

$$\int_0^{2\pi} d\psi \cos^3 \psi = 0. \quad (3.16)$$

In other words, when the wave distribution is perfectly isotropic, the spectral coherence between tilt and strain is zero. The same result holds for compressional waves as well. It shows that we need anisotropy in order to use the relation between tilt and strain to characterize the ice motion. Given anisotropy, analysis of the cross spectra yields the desired dispersion relation. Comparison of the dispersion relation to the forms expected for flexural and compressional waves allows estimation of their relative magnitudes.

### 3.6.2 Internal wave packet

Figure 3.20 shows time series of strain measured by the rosette near mooring I1, beginning at 22:43 on 17 April. The record includes the apparent internal wave packet measured by the tiltmeters and shown in Figure 3.13. Strain in the direction 120° east of magnetic north is anticorrelated with strains along 0° and 240°. Compressional waves generate nondeviatoric strains (the sum of principal strains is zero), so one axis must be anticorrelated with the other two. Hence the records show that strains at frequencies below 10 mHz or so are predominantly the result of compressional, not flexural, activity.

The time series do not reveal the clear wave packet-like signal shown by tilt. Examination of time series of water temperature at constant depth beneath the ice, collected in the Levine/Paulson mooring array, shows that water motion correlates better with tilt than with strain. Figure 3.21 shows simultaneous time series of temperature at a depth of 99.5 m, surface tilt, and surface strain measured by sensors at mooring I1. The mixed layer fortuitously happens to be of the order of 100 m deep. Hence, before the arrival of the wave packet, the thermistor sits in the mixed layer where the vertical temperature gradient is small. The packet's arrival makes the mixed layer shallower, indicated by the sharp break in the signal just after midnight. Fluctuating water motion is revealed by temperature variations thanks to the larger gradient.

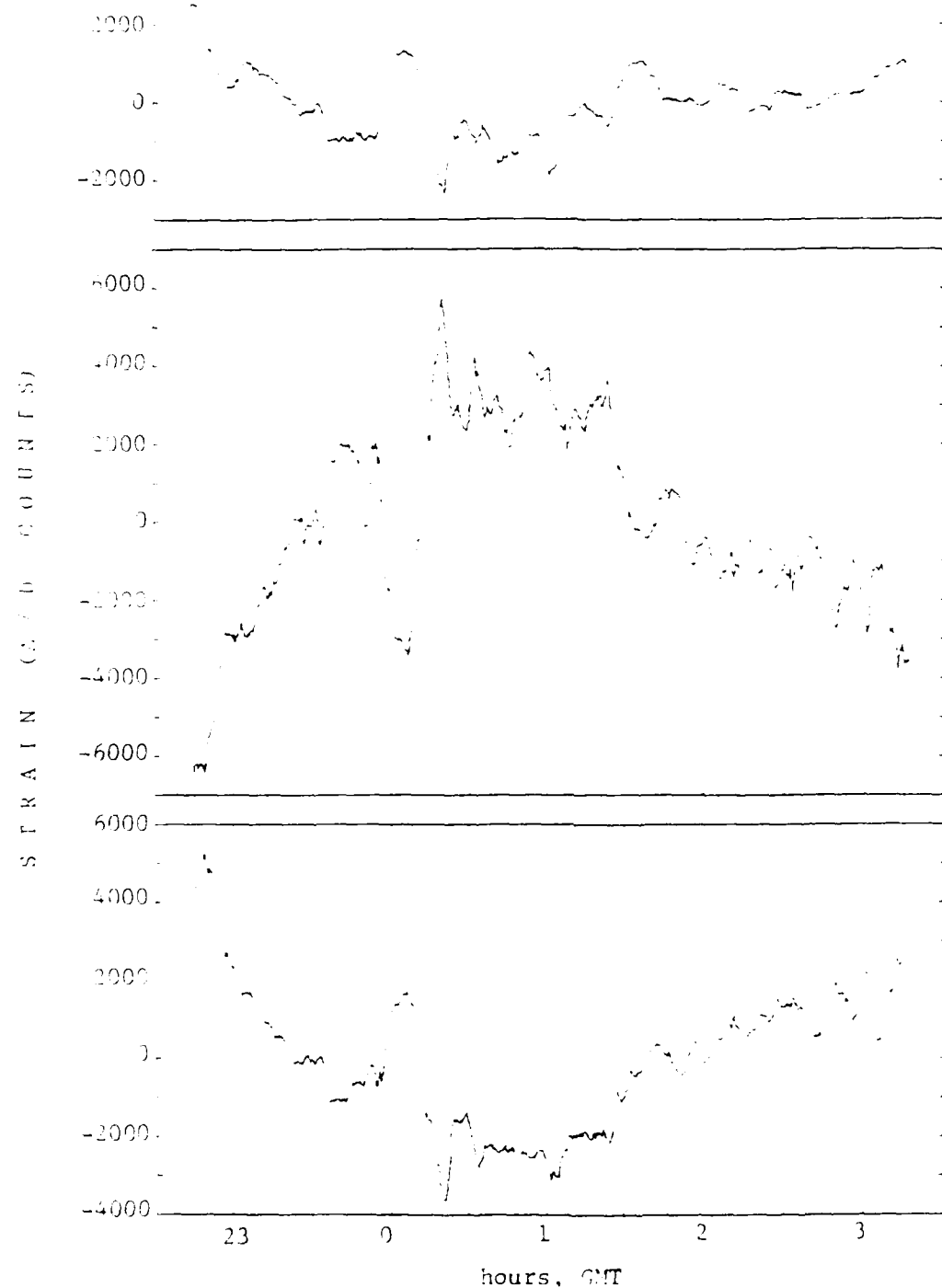
These fluctuations correlate well with the tiltmeter record. Examination of the cross spectrum shows the relative phase to be  $\pi/2$ , consistent with the fact that tilt is the derivative of vertical displacement. Analysis of the lags of temperature across the inner mooring array yield a wave heading of 20 degrees true, a wavelength of 650 m, and a phase speed of 0.46 m/sec, all in good agreement with the tiltmeter results.

By contrast, cross spectral analysis between strain and temperature shows poor coherence. It is tantalizing to speculate, however, that the notable "bump" in the strain time series may be a consequence of the mixed layer becoming shallower. Conversely, it is somewhat mysterious that the tiltmeter time series does not show a response to that event, but only to the subsequent oscillations. However, it appears that tilt records show the influence of internal waves on the surface, while strain is dominated by compression caused perhaps by differential motions of the ice pack.

Quantitative comparison of measured surface displacement to internal wave model predictions requires that water displacements be known. This in turn requires CTD cast profiles to turn variations of temperature at constant depth to variations of isotherm depth. Further investigation of tilt and strain response to internal waves also requires examination of response to other internal wave trains recorded during CEAREX.

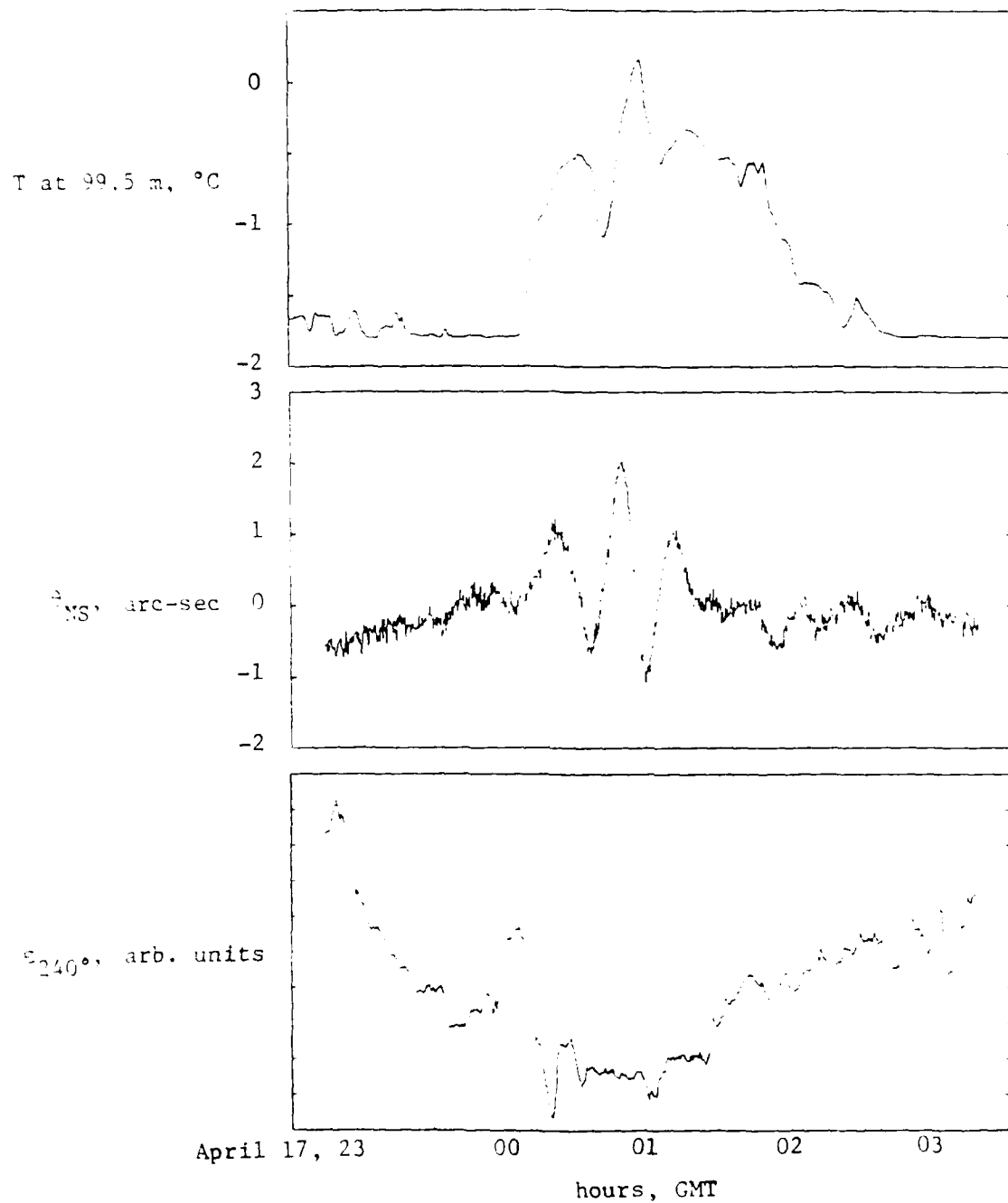
## 3.7 Time series and spectra of ice events

A first examination of tiltmeter time series reveals at least two types of signals not associated either with swell or with internal waves. One signal is characterized by an impulsive onset followed by a damped sinusoidal decay that occurs simultaneously, within measurement capability, on all three tiltmeters. The other type is a rapid oscillation that builds over a few cycles, may be sustained for an extended time, and decays over several cycles. The oscillation period, about a few seconds, is distinctly shorter than the usual swell. We tentatively identify the first type of signal with ice rupture or cracking, and the second with floe oscillations. We discuss each in turn. We also mention two known signal sources: landings and takeoffs of the Twin Otter aircraft, and air gun discharges.



**FIGURE 3.20**

Time series of strain near mooring II and tiltmeter 180, beginning at 23:43 on 17 April. Top, strain along magnetic north; center, strain  $120^{\circ}$  east of magnetic north; bottom, strain  $240^{\circ}$  east of magnetic north. Calibration in strain units awaits information from SPRI. Anticorrelation of the center record with respect to the other two indicates that strain is compressive; the same records are all in phase at infra-swell periods, indicating that swell causes flexure.

**FIGURE 3.21**

Water temperature at a depth of 99.5 m (top), ice tilt in the north-south plane (center), and ice strain along a direction 240° east of north (bottom), near mooring II. Tiltmeter fluctuations are well-correlated to internal waves measured by the thermistor. Strainmeter fluctuations are poorly correlated, and may be dominated by strains from differential motion of the ice pack.

### 3.7.1 Ice rupture events

Figure 3.22 shows time series for the six tiltmeter axes of a rupture event occurring on 10 April at 23:57 UT. Superimposed on the swell signal that usually dominates the record are a number of features. A very rapid oscillation precedes a sharp spike followed by a decaying sinusoidal oscillation. The behavior occurs three times in the interval, the second being the largest occurrence. Spectral analysis of coherence between the three tiltmeters shows no phase lag between them. In the time domain, the sampling rate of 1 Hz is too coarse to allow estimation of a time lag between tiltmeters that would allow determination of the propagation direction and origin of the signal.

We tentatively identify this signal, and others like it, as seismic P and/or S waves in the ice, generated by ice rupture ("ice quakes"). Impacts from distant ice ridging or rafting events may also cause these signals; an interesting task will be to examine whether other such events in the record display similar clustering of several impulses within some characteristic time span, suggestive of floes jostling each other repeatedly [P. Wadhams, personal communication]. Using the speed of sound in ice, roughly 5000 m/sec, we find that the maximum arrival time delay in the tiltmeter array is

$$\Delta\tau \approx \frac{13.5 \text{ m}}{5000 \text{ m/sec}} = 0.03 \text{ sec}, \quad (3.17)$$

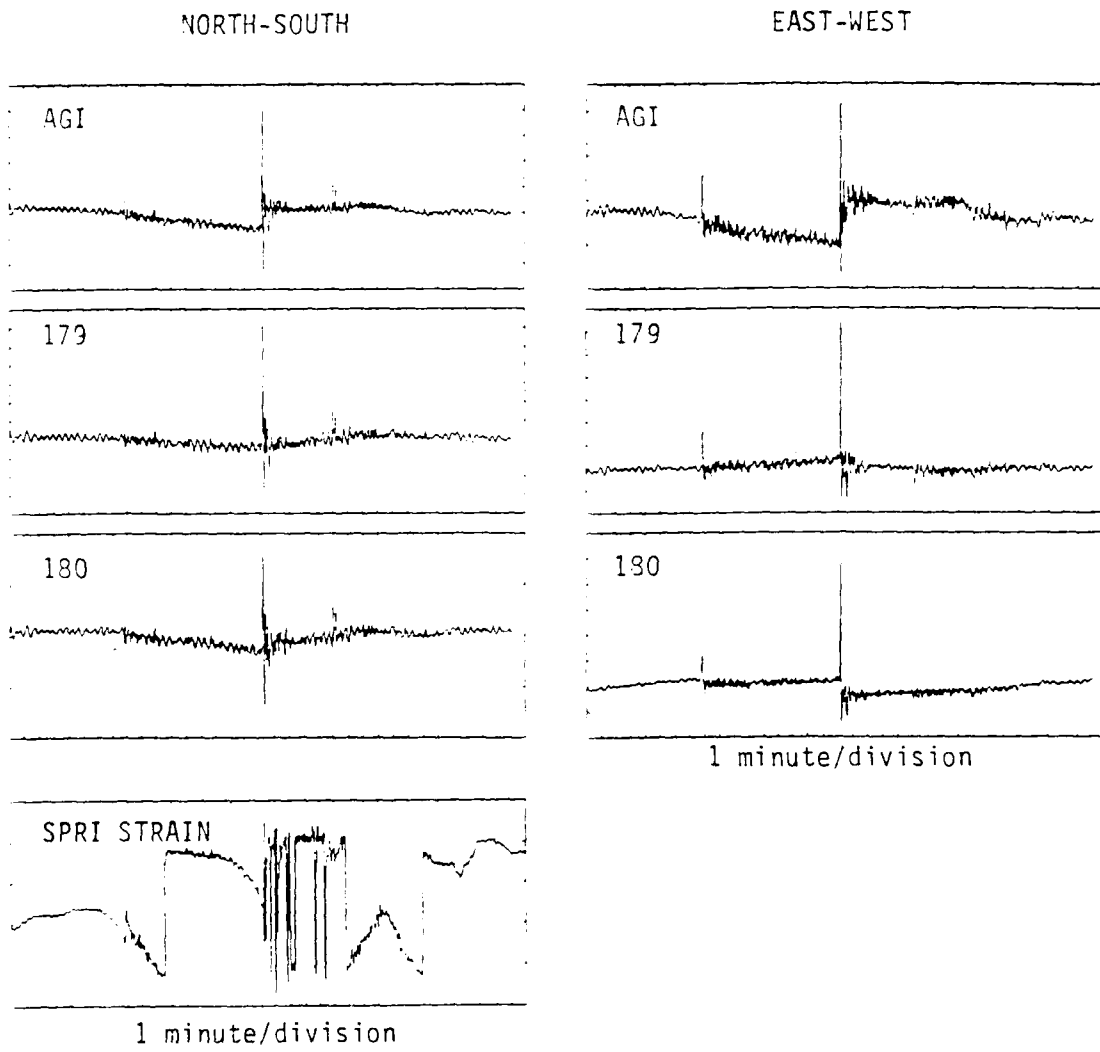
indeed too short to be resolved by our sampling rate. We discount the possibility that the signal is artificial because most human activity at the camp cannot be detected unless it occurs within a few feet of a tiltmeter, and these signals appear simultaneously at all three points of the array. Furthermore, this particular event occurred near midnight when the activity level is low.

Wind-induced ice fracture may also explain the signal [P. Wadhams, personal communication]. Wind drag on the ice causes the ice to tilt downwind. When stress caused by hydrostatic imbalance exceeds the failure strength of the ice, it breaks in an array of cracks perpendicular to wind direction. The distance between cracks varies inversely with wind speed. Further analysis of similar signals requires correlating them to episodes of elevated wind speed, or to gusts of wind. Data will be available from the Naval Postgraduate School meteorology group of K. Davidson and P. Guest.

The spiky character of the ice quake signal alters the spectrum of ambient tilt fluctuations by adding white (or pink) noise. Figure 3.23 shows that the added noise fills in the spectral valley between the internal wave rise and the swell peak. The SPRI analog recording system offers broadband capability that may reveal interesting high-frequency characteristics of the signal; however, the SPRI sensor data may be adversely affected by slow servo motor response during this episode. Nevertheless, accurate measurement of onset times is possible using the analog data, allowing the direction of the source to be determined.

### 3.7.2 Rapid ice oscillations

Figure 3.24 shows a time series segment from April 2. Superimposed on the usual swell is a more rapid oscillation that grows within a few cycles to a steady amplitude and then decays after a while. The signal appears on all tiltmeters. The figure shows an oscillation orientation that changes with time during the record. A central section shows increased east-west activity coincident with decreased north-south activity, compared to other parts of the episode.

**FIGURE 3.22**

Thirty-minute long time series of the six axes of all three tiltmeters, starting at 23:40 hours on 10 April. The left-hand column displays north-south tilt fluctuations, and the right-hand column displays east-west fluctuations. Also shown is the north-south SPR1 strainmeter channel, which reveals a coincident disturbance as well as servo offsets. Note the secular tilt preceding the "main shock", followed by a recovery either instantaneous with the shock or gradual, following the shock.

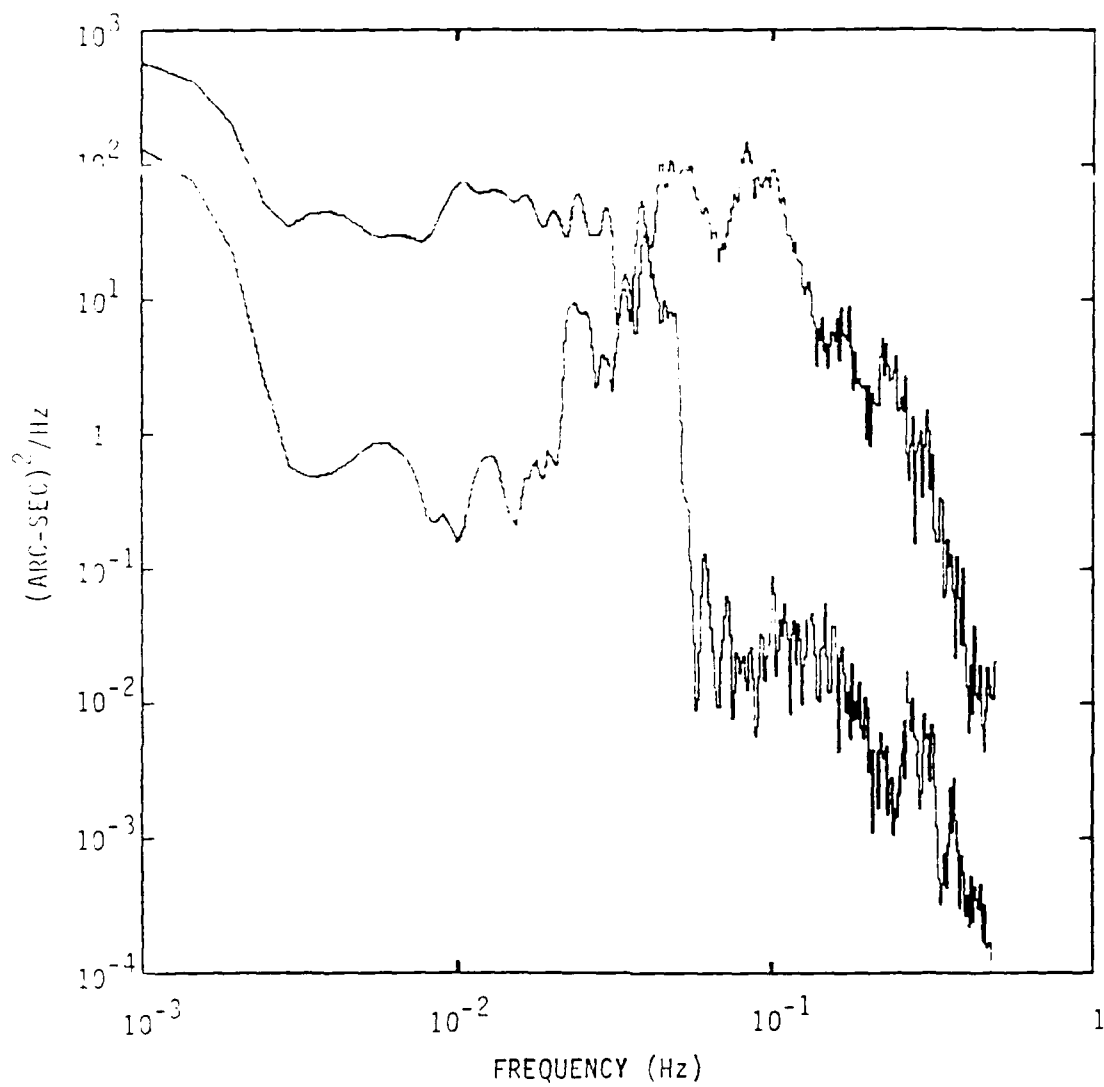


**FIGURE 3.29**

Spectra of 34-minute records of north-south tilt measured by tiltmeter 179. The bottom spectrum reflects the time series ending at 23:43 on 10 April, just before the "ice quake" events. The long-period swell peak and spectral valley are easily discerned. The top spectrum, of a time series centered on the "main shock", shows white noise filling the spectral valley and even swamping the swell peak.

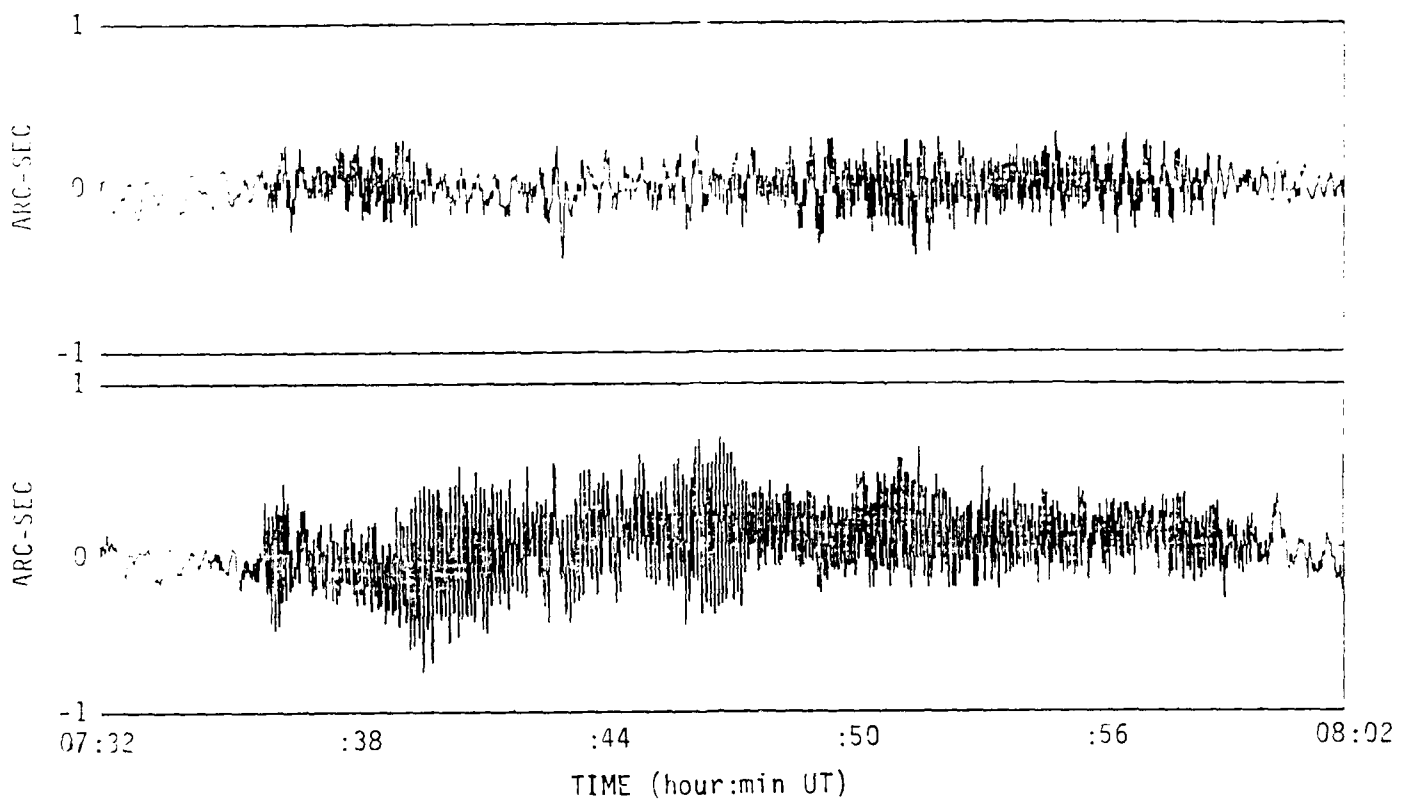


**FIGURE 3.24**

Time series of north-south (top) and east-west tilt fluctuations starting at 07:32 hours on 2 April, measured by tiltmeter 179. High frequency oscillations are superimposed on the swell signal. The oscillations vary in orientation, becoming almost purely east-west for a period near the center of the record.

**Figure 3.25** shows power spectra of the orthogonal axes of tiltmeter 179. The short record makes the long-period swell peak poorly resolved, though distinct. Unlike the white noise characteristic of the rupture events of section 3.7.1, these spectra reveal several well-defined peaks. The most prominent peaks appear at periods of 6.2 and 5.0 sec; other peaks can be discerned at periods of 3.0 and 2.5 sec.

**Figure 3.26** displays results of cross spectral analysis of the segment. It shows high coherence at periods around 5 and 6 seconds. The phase between orthogonal axes at these periods is nonzero, consistent with the changing orientation of the tilt vector.

Several mechanisms can generate high frequency waves. For example, consideration of the restoring forces on an ice floe displaced vertically from hydrostatic equilibrium lead to an approximate value for the resonant frequency of bobbing of the floe:

$$\omega_{\text{bobbing}} \approx \sqrt{g(\rho_w - \rho_i)/h\rho_i}, \quad (3.18a)$$

where  $g$  is the acceleration of gravity,  $h$  is the average thickness of the floe, and  $\rho_w$  and  $\rho_i$  are the density of sea water and sea ice, respectively. Inserting typical values for density and choosing  $h = 2.5$  m, we find the bobbing period  $T_b = 2\pi/\omega_b \approx 9.5$  sec. Thus, bobbing of the floe, initiated by a ridging event, lead formation, or wind, causes oscillations of about the right frequency.

Similarly, rocking an ice floe about its center of buoyancy produces a resonance in the right range of periods. The resonant rocking frequency of a uniform, rectangular floe is approximated by

$$\omega_{\text{rocking}} \approx \sqrt{g\rho_w/2h\rho_i}, \quad (3.18b)$$

yielding a rocking period  $T_r$  of about 4.3 sec, using the same parameters as above. The values for bobbing and rocking fall into the right range to explain the observed excitations.

Other potential mechanisms for the signal are short-period swell excited on open leads by wind, and also flexural-gravity waves excited by wind acting directly on the ice [Wadhams, 1986]. Hunkins [1962] tentatively concluded that he observed wave excitations when the wind speed exceeded 12 m/sec. Wadhams [1986] and Squire [1989] show that waves are excited only when wind speed exceeds a critical value, namely the minimum in the group speed-wave period dispersion relation for flexural-gravity waves. Resulting waves are strongly peaked at the period corresponding to this minimum. The speed and period of the minimum depend on ice thickness. From Figure B.5 of Wadhams [1986], we read off values of the minima for different ice thicknesses. For ice one meter thick, the minimum wind speed for wave excitation is 12 m/sec and the resulting period is 12 sec. Extrapolating from the few points of the graph, a period in the range between 5 and 6 seconds corresponds to an ice thickness of 30 to 45 cm and requires a wind speed in excess of about 10 m/sec.

The ice at O-camp, averaging 2 to 3 m in thickness, is clearly too thick to explain these oscillations as the result of strictly local forcing. However, helicopter operations around camp confirm that camp was surrounded within one or two kilometers on any side by recently refrozen leads or even open leads [D. Robertson, personal communication]. Thus, sufficiently thin ice existed nearby where waves could have been forced, propagating into the thicker floe of O-camp. Personal experience with severe cold from high winds on 2 April confirms strong, gusty wind conditions. Correlating this and other episodes of high frequency ice oscillation with time series of wind speed will test hypotheses of flexural-gravity wave forcing by wind.

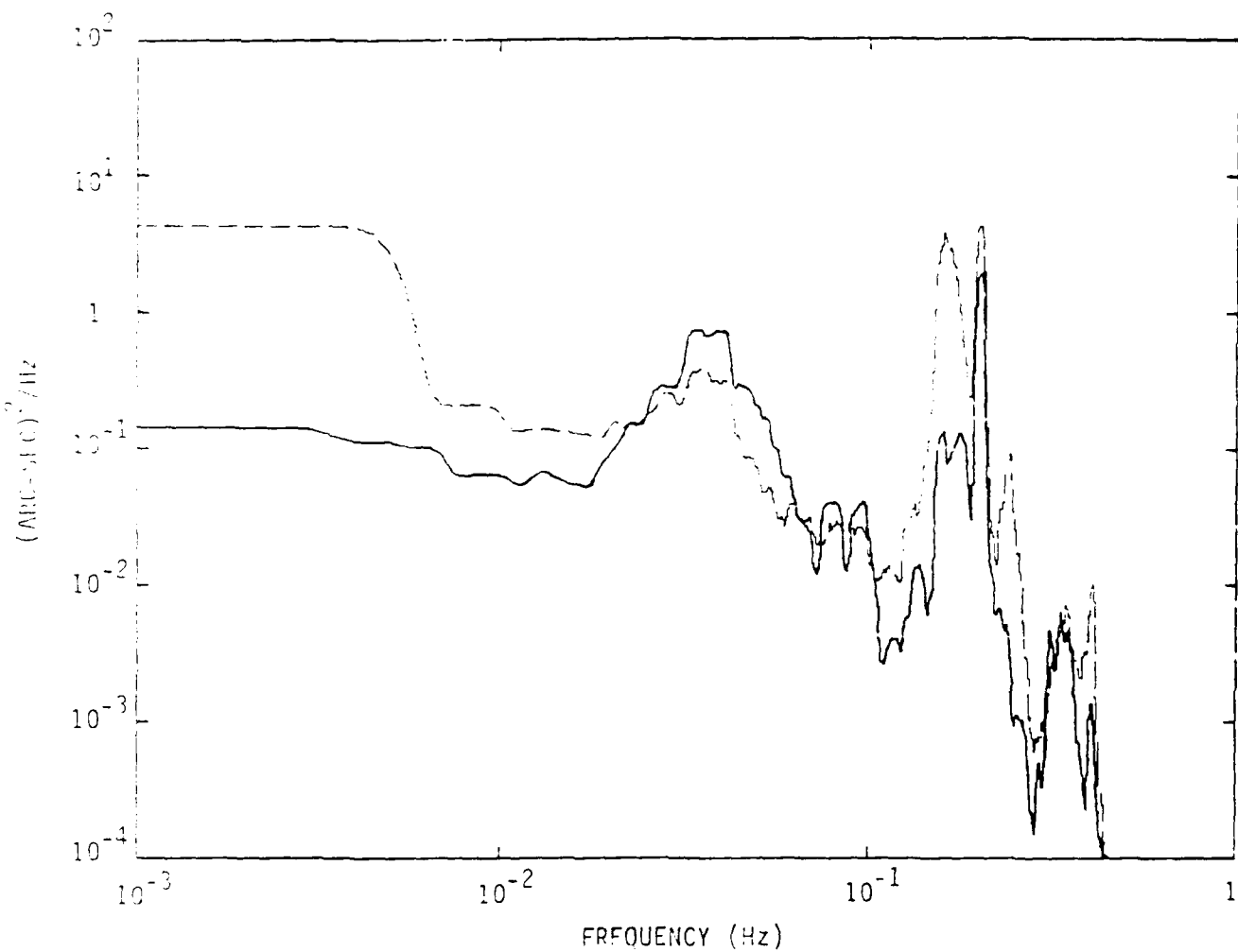


**FIGURE 3.25**

Spectra of the north-south tilts (solid trace) and east-west tilts (dashed trace) of Figure 3.24. The swell peak remains clearly discernible during the oscillation event, which excites well-defined resonant peaks with periods of 6.2, 5.0, 3.0, and 2.5 seconds.

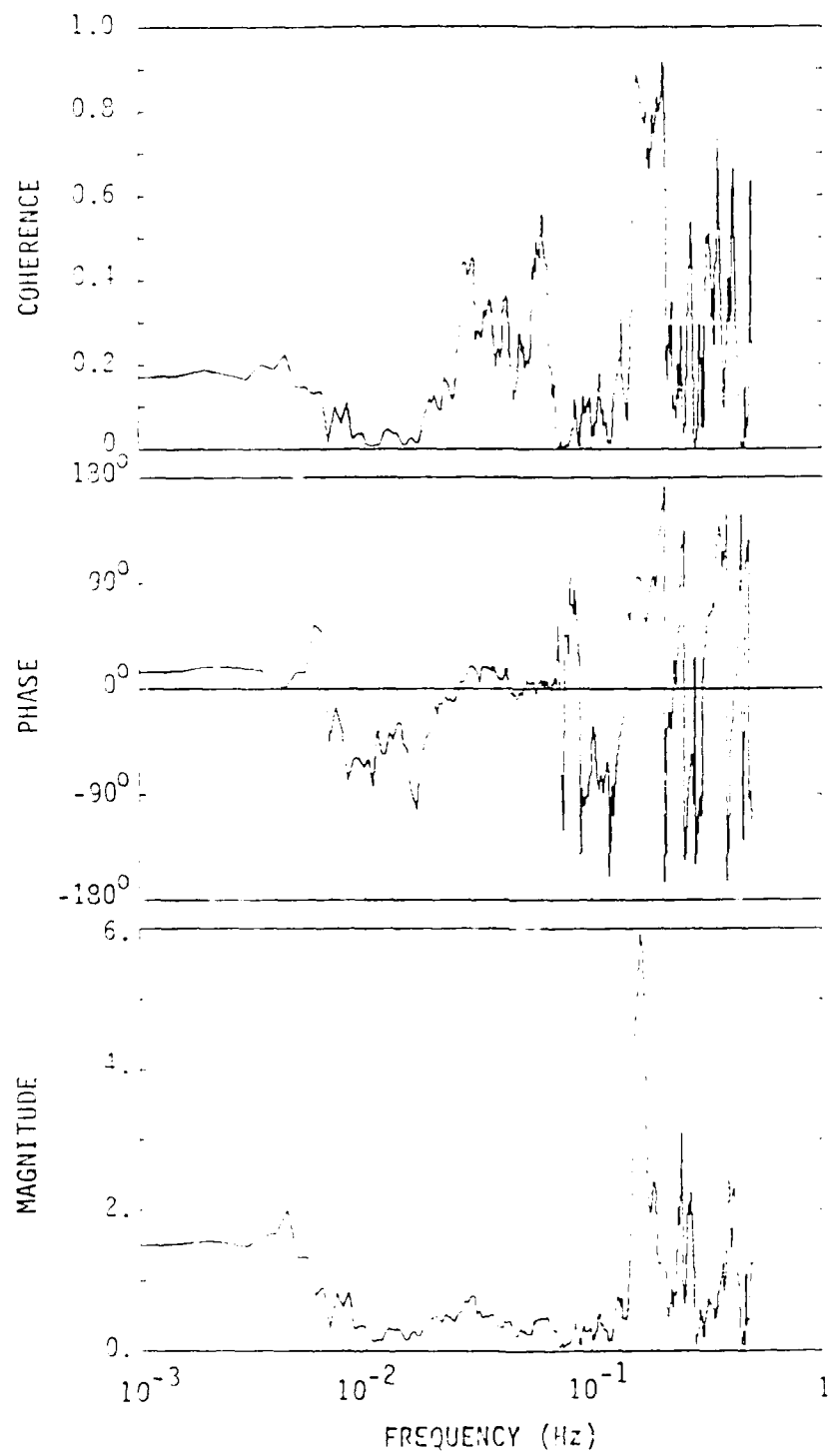


**FIGURE 3.26**

Cross-spectral results, averaged over 21 spectral points or a 10 mHz bandwidth, of the tiltmeter records of Figure 3.24. High coherence is shown for the band around the 6.2 sec and 5 sec peaks; the phase is nonzero as predicted for multidirectional excitations.

### 3.7.3 Airplane landings

Airplanes landing and taking off on the ice generate a third type of signal. A plane moving on the ice is a moving load which generates propagating flexural waves. The literature on ice response to moving loads is old and rich, given that the subject is of practical importance both to ice skaters and to airplane safety on Arctic ice floes. A recent experimental and theoretical study of waves generated by moving loads is given by *Takizawa* [1988].

Observation of unfiltered tiltmeter outputs on a stripchart recorder at the O-camp showed that the airplane generates large-amplitude, high-frequency flexural waves in the ice [*S. Moore*, personal communication]. However, a look at tilt data around the time of landing on 19 April suggests that wave frequencies largely fall outside the bandwidth of our digital records.

**Table 6** is a log of Twin Otter flights involving O-camp landings. The time of day of ice camp landings and takeoffs are not available at this point, and must be obtained from Bradley Air Services. In the Table, Longyearbyen airport is denoted by its international call letters, LYR; the letters O and A denote O-camp and A-camp, respectively; and Nord denotes Nord Air Base in Greenland. Detailed examination of all records at the time of Twin Otter landings will clarify whether they contribute noise within the digitally sampled bandwidth.

**TABLE 6.**  
*TWIN OTTER FLIGHT LOG*

<u>DATE</u>	<u>FLIGHT</u>
3/28	LYR - O - LYR
3/29	LYR - O - LYR
4/02	LYR - A - O - A - LYR
4/04	LYR - O - A - Nord - A - O - LYR
4/05	LYR - O - LYR
4/09	LYR - A - O - LYR
4/10	LYR - O - LYR
4/11	LYR - A - O - LYR
4/12	LYR - O - LYR - O - LYR
4/15	LYR - O - A - O - LYR
4/16	LYR - O - A
4/17	A - reconnaissance - A - LYR - O - LYR
4/18	LYR - O - A - LYR
4/19	LYR - O - LYR - A - LYR - O - LYR

### 3.7.4 Air gun discharges

The air gun used as an underwater acoustic source for long-range transmission experiments was set up in a hut about 500 m NW of the tiltmeter array. The gun source was suspended some 10 m beneath the ice and set off every minute or so. The air gun operated on 16 April from 20:30 to 22:30 and on 17 April from about 09:00 to 24:00. The dominant signal frequency is 15 Hz, the breathing mode of the air bubble generated by the gun. We also expect a broadband, pulse-like component. Neither the digital records nor direct inspection of unfiltered outputs on the stripchart recorder at camp show a signal correlated to the air gun bursts [*R. Williams*, personal communication]. The source is evidently too weak to generate measurable flexure of the ice.

## 4.0 SCIENTIFIC ISSUES AND REQUIRED ANALYSES

The review of Section 3 shows that the CEAREX tiltmeter array produced a substantial body of data of excellent quality. Overall spectral characteristics are similar to those measured earlier on the Beaufort Sea. Tilt fluctuations from swell and from internal wave-like oscillations have been identified. The origin of incident swell recorded during one segment has been shown to be the Atlantic south of the Fram Strait. In addition, other events have been identified that may be caused by ruptures in the ice and by locally induced floe oscillations.

Analysis of the tiltmeter data has answered many questions. Some questions remain open, however, and new ones are raised. In this section, we discuss scientific issues that can be resolved by further study of the data set in conjunction with data from oceanographic and meteorological measurements.

### 4.1 Spectral variability over different time scales

The pack ice provides a highly stable platform from which to make oceanographic and other measurements. The degree of stability is quantified by spectra of tilt fluctuations caused by the natural background. An issue requiring resolution is to determine variability of the background. Ultimately, we wish to learn about seasonal variability. However, since both AIWEX and CEAREX data were taken during the Arctic spring, this is not an attainable goal at present.

Nevertheless, by compiling a complete catalog of overlapping spectra, we can reliably characterize springtime variability of ice motions in the bandwidth 0.1 mHz to 0.5 Hz in two regions of the Arctic. Analysis can confirm or dismiss the intuition that the greater shear in the eastern Arctic causes higher variability compared to the Beaufort Sea.

Another issue is to what extent spectral variability depends on the length of the time series analyzed. Shorter records, appropriate for investigating short-lived phenomena, are expected to display greater variability. Analysis of the complete data set using segments of different lengths quantifies the dependence of variability on record length.

### 4.2 Internal wave and swell studies

In order to obtain point measurements of the dispersion relation for waves propagating in the ice, we must reduce the SPRI strainmeter data and perform cross-spectral analyses with data from the colocated tiltmeter. Strainmeter data reduction is tedious and time-consuming because of the numerous offsets introduced by the resetting servo motor. It is crucial, however, to measure dispersion and to resolve whether internal wave dissipation generates compressional waves in the ice.

Analysis of the tiltmeter array data provides a spatially averaged measure of wave dispersion in the ice. It also allows measurement of the changing directionality of the swell and internal wave fields.

Most importantly, detailed data analysis must be aided by other data from the O-camp. A record of camp drift, together with data on depth and stratification of the mixed layer, allows investigation of the generation of internal wakes by pressure ridge

keels. Camp drift heading determines the plane in which the ice is expected to pitch as the wake is generated. Mixed layer information allows estimates of the expected intensity of keel wakes. Drift information will be made available by the Polar Science Center. Mixed layer stratification was measured using CTD casts by J. Morison.

Scientists at the O-camp reported occasional observation of strong semidiurnal oscillations in the water [T. Dillon, L. Padman, R. Pinkel, personal communications]. Oscillation amplitude typically peaked following days of strong wind or storms. Concatenation of the tiltmeter and strainmeter files into continuous records spanning several days will allow first measurements of ice response to internal oscillations approaching inertial frequency, as well as of tilts caused by the ocean tides.

#### 4.3 Flexural and compressional waves

Inspection of strain meter stripchart records at the O-camp confirms that at internal wave frequencies, one strainmeter axis is  $180^{\circ}$  out of phase with the other two in a rosette. At frequencies of several tens of mHz, corresponding to long-period swell, all three strain axes are in phase. This means that at internal wave frequencies, ice strain is predominantly compressional, and in the swell band, flexural. Study of the strainmeter data together with the tiltmeter data during quiescent periods as well as during passage of internal wave packets can test the hypothesis, supported by examination of one packet, that ice strain at internal wave frequencies results from mechanisms, other than internal waves, that drive differential motion of the ice pack. Comparison of ice motion to measurements of current just beneath the ice by M. McPhee can answer questions about the drag coefficient of the ice and excitation of compressional waves in it. Comparison of tiltmeter/strainmeter time series and spectra with those of the colocated moorings of M. Levine and C. Paulson enables study of the coherence between internal wave oscillations at depth and resulting surface displacements.

#### 4.4 Ice events and local forcing of waves by wind

A complete catalog of anomalous ice events is necessary to validate our tentative classifications of them and to characterize them. Phase speed of waves travelling through the array can separate high-speed seismic-like waves from slower flexural waves. Examination of the grouping of "ice quakes" in time can determine whether they occur with any regularity. Accumulation of anecdotal evidence, such as helicopter pilots' reports of new lead formation around camp, can help decide whether some events are related to lead formation or other local ice dynamics. Similarly, an accurate log of airplane landing and takeoff times, maintained by the air crew, can pinpoint sections of data to investigate whether aircraft-generated flexural signals extend into the record bandwidth. Most importantly, comparison of the data to local meteorological data, particularly time series of wind speed and direction collected by P. Guest, can shed light on the open question of local wind forcing of flexural waves in the ice. The possibility that some signals result from thermal cracking of the ice can be studied using Guest's records of air temperature, our records of temperature under the snow cover, and R. Colony's records of the temperature profile in the ice.

#### 4.5 Tilt amplitude anomaly

The discussion of section 3.4 raises the possibility that tilting of the ice in response to long waves may not simply reflect tilt of a free surface. Rather, it may be affected by local variations in ice thickness and rigidity. These variations may in turn affect the dispersion of long waves in a heretofore unexpected way. In order to confirm these conclusions, we must demonstrate that the difference in tilt amplitudes measured by the array are not an instrumental artifact. Recalibration of the tiltmeters and data acquisition system is not likely to explain factors of two in amplitude response. If the SPRI strainmeter array shows similar amplitude differences, it will confirm that our result is inherent in the ice response. Further work to resolve the issue thus involves close collaboration with the SPRI group.

#### 4.6 Directional spectral analyses

Preliminary directional analysis reported in Section 3.5 only applies in the special case when the local wave field is dominated by waves from a single source at each frequency. More general analyses can determine wave headings when the field is made up of waves from more than one origin. For example, we can reconstruct tilt projections along arbitrary directions by appropriate summation of the measured orthogonal tilt components. Spectra of projections can be used to make plots of power at a given frequency versus heading angle. Waves from a single source generate polar plots with single lobes, and waves from multiple origins generate multi-lobe plots.

Directional analysis can yield spectral relations in different directions, distinguishing, for example, waves forced locally by wind (which cluster at periods corresponding to the phase speed minimum for flexural-gravity waves) from infra-swell originating far away. Alternatively, a heading-dependent dispersion will confirm the possibility, raised by the tilt amplitude anomaly, that local variations in ice thickness and rigidity affect the propagation even of waves much longer than the ice thickness. Finally, directional analysis may be able to separate out internal waves created by ice drift from the ambient internal wave field.

## 5.0 CONCLUSION

The CEAREX tiltmeter array experiment successfully generated significant data of high quality. Preliminary analyses already confirm qualitatively the common (if not universal) shape of the ambient tilt spectrum between 0.1 mHz and 500 mHz. A rise in signal power occurs below a frequency corresponding to the local maximum in the Brunt-Väisälä frequency. A broad spectral peak around 30 mHz represents filtered long-period swell propagating from the open ocean. The swell peak and the internal wave rise are separated by a spectral valley or window.

Analyses also reveal the greater dynamic activity in springtime of ice north of Fram Strait, compared to the Beaufort Sea. Analysis of swell incident on the array during one 9-hour period shows that it is dominated by waves originating in the north Atlantic, reaching the O-camp through the Fram Strait. Variation of heading with frequency is consistent with damping determined by distance travelled through intervening ice.

Detailed analysis of the tiltmeter data, in conjunction with oceanographic and meteorological records, offers the potential to resolve several outstanding puzzles in Arctic physical oceanography. Reduction of strainmeter data allows measurement of the dispersion relation governing swell-induced flexural wave propagation through the ice. It also tests hypotheses about the mechanisms driving compressional strains in the ice at internal wave frequencies. Taking tilt, strain, and oceanographic data in concert with records of translational velocity can show under what conditions ice drift can lead to internal wave generation by ice keels. Together with time series of local wind, the data can describe conditions leading to flexural wave forcing by wind.

Together with oceanographic data, the tiltmeter and strainmeter data characterize the interaction between the liquid and solid ocean more completely than ever before. They may enable a new understanding of the mechanisms governing the dissipation of internal waves in the Arctic Ocean.

## 6.0 REFERENCES

American Geographical Society, Map of the Arctic region, Scale=1:5,000,000, 1975.

Andersen, R., CEAREX O-camp azimuth record, Polar Science Center, Seattle, 1989.

CEAREX Situation Report No. 31, Tromso CEAREX Office, 3 April 1989.

Czipott, P.V., and W.N. Podney, Measurement of magnetic fluctuations above the Arctic Ocean during project AIWEX: Experiment description and data overview, Physical Dynamics Report No. PD-LJ-85-341R, 1985.

Doronin, Y.P., and D.E. Kheisin, **Sea Ice**, Amerind Publishing Co. Pvt. Ltd., New Delhi, 1977.

Hunkins, K., Waves on the Arctic Ocean, *J. Geophys. Res.* **67**, 2477–2489, 1962.

Kolsky, H., **Stress Waves in Solids**, Dover Publications Inc., New York, 1963.

Manley, T.O., L.A. Codispoti, K.L. Hunkins, H.R. Jackson, E.P. Jones, V. Lee, S. Moore, J. Morison, T.T. Packard, and P. Wadhams, The *Fram 3* expedition, *EOS Trans. AGU* **63**, 627–636, 1982.

Munk, W.H., Long ocean waves, in **The Sea**, ed. M.N. Hill, Wiley, New York, Vol. 1, 647–663, 1962.

Phillips, O.M., **The Dynamics of the Upper Ocean**, Cambridge University Press, Cambridge, pp. 206–217, 1980.

Podney, W.N., and P.V. Czipott, Tiltmeter measurements of internal wave spectra, *EOS Trans. AGU* **67**, 1052, 1986.

Sommerfeld, A., **Mechanics of Deformable Bodies**, Academic Press, New York, 1950.

Squire, V.A., *J. Geophys. Res.*, in press, 1989.

Takizawa, T., Response of a floating sea ice sheet to a steadily moving load, *J. Geophys. Res.* **93**, 5100–5112, 1988.

Wadhams, P., The seasonal ice zone, in **The Geophysics of Sea Ice**, ed. N. Untersteiner, Plenum Publishing Corp., New York, 825–991, 1986.

Williams, R., S. Moore, P. Wadhams, and M. Beard, Measurements of strain in sea ice during *Fram 3*, Scott Polar Research Institute Technical Report 89–1, 1989.